iScience

CellPress
OPEN ACCESS

Article

A nonhuman primate model of vertical sleeve gastrectomy facilitates mechanistic and translational research in human obesity

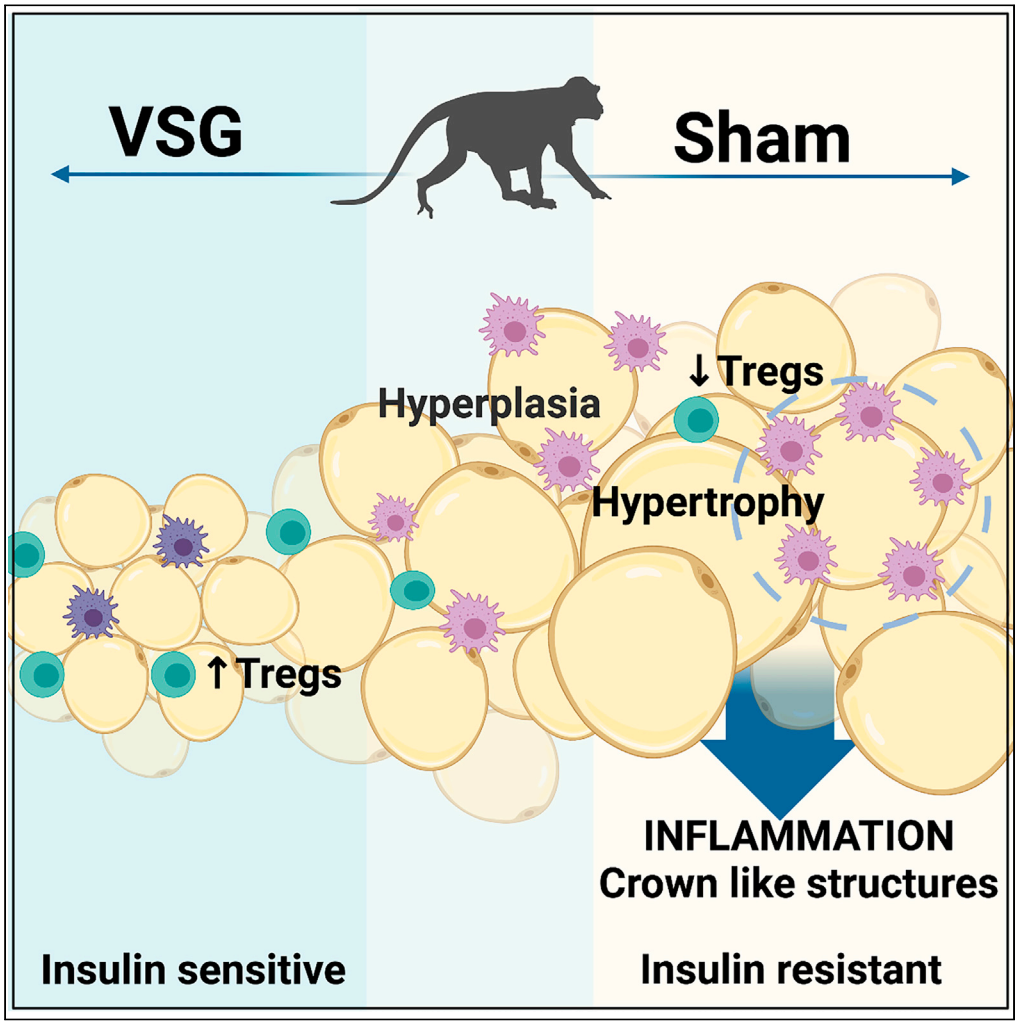

Julia L. Nugent, Amar Singh, Keith M. Wirth, ..., Sabarinathan Ramachandran, Sayeed Ikramuddin, Melanie L. Graham

graha066@umn.edu (M.L.G.)
sramacha@umn.edu (S.R.)
ikram001@umn.edu (S.I.)

Highlights

A monkey model of vertical sleeve gastrectomy (VSG) accurately mimics human VSG

VSG confers durable metabolic benefits

VSG decreases crown-like structure density and alters macrophage phenotype

Interplay of metabolites and immune cell populations in VSG

Nugent et al., iScience 24, 103421
December 17, 2021
https://doi.org/10.1016/j.isci.2021.103421

iScience

CellPress
OPEN ACCESS

Article

A nonhuman primate model of vertical sleeve gastrectomy facilitates mechanistic and translational research in human obesity

Julia L. Nugent,[1,2] Amar Singh,[1,3] Keith M. Wirth,[1] Scott Hunter Oppler,[1,2] Laura Hocum Stone,[1,2] Jody L. Janecek,[1,2] Adam C. Sheka,[1] Scott Kizy,[1] Meghan E.G. Moore,[1,2] Christopher Staley,[1,4] Bernhard J. Hering,[1,3] Sabarinathan Ramachandran,[1,3,*] Sayeed Ikramuddin,[1,*] and Melanie L. Graham[1,2,5,*]

SUMMARY

The obesity epidemic significantly contributes to overall morbidity and mortality. Bariatric surgery is the gold standard treatment for obesity and metabolic dysfunction, yet the mechanisms by which it exerts metabolic benefit remain unclear. Here, we demonstrate a model of vertical sleeve gastrectomy (VSG) in nonhuman primates (NHP) that mimics the complexity and outcomes in humans. We also show that VSG confers weight loss and durable metabolic benefit, where equivalent caloric intake in shams resulted in significant weight gain following surgery. Furthermore, we show that VSG is associated with early, weight-independent increases in bile acids, short-chain fatty acids, and reduced visceral adipose tissue (VAT) inflammation with a polarization of VAT-resident immunocytes toward highly regulatory myeloid cells and Tregs. These data demonstrate that this strongly translational NHP model can be used to interrogate factors driving successful intervention to unravel the interplay between physiologic systems and improve therapies for obesity and metabolic syndrome.

INTRODUCTION

Obesity affects 42% of Americans and 13% of adults worldwide (Kumanyika and Dietz, 2020; WHO, 2020). Obesity is responsible for 40% of cases of cardiovascular disease, most type 2 diabetes (T2D), 10–41% of some cancers, and a significant burden of neurodegenerative disease, resulting in higher rates of disease morbidity and all-cause mortality in the metabolically unhealthy obese (MUO) population (Ahima and Lazar, 2013; Kumanyika and Dietz, 2020). In contrast with MUO, metabolically healthy obese people (MHO) have reduced risks, morbidity, and mortality similar to that of people who are lean and metabolically healthy (Phillips, 2017). Although most obesity outcomes historically have focused on weight, this suggests that a shift toward evaluating metabolic health independent of weight is more relevant to long-term health. Phenotypic differences between MUO and MHO populations are underscored by translational and clinical studies linking "central obesity," or accumulation of visceral adipose tissue (VAT), such as the omentum, as a key factor in developing the metabolic syndrome (MetS), which is a spectrum of diseases including T2D, hypertension, hyperlipidemia, nonalcoholic steatohepatitis, and cardiovascular disease, that develop independent of body mass index (BMI) (Fox et al., 2007; Ooi et al., 2019).

Initial treatment for obesity and the MetS is typically lifestyle intervention to include more exercise and healthier dietary choices, concurrent with or followed by medical management with anti-hypertensives, statins, and oral antihyperglycemics and/or insulin if diabetes develops (Association, 2018a, 2018b). Despite the initial effectiveness of these interventions, there is often poor long-term adherence to lifestyle interventions and many people regain weight (Wing et al., 2013). Pharmaceutical therapies for obesity have proven mostly limited in their ability to induce weight loss, with the majority of medications generally reducing body weight by about 5% (Bersoux et al., 2017; Khera et al., 2016; Yanovski and Yanovski, 2021), though GLP-1 receptor agonists have resulted in losses of 5–10% in many patients, and up to 20% in a small subset of patients (O'Neil et al., 2018). Furthermore, these medications require long term use to maintain effectiveness, are cost-prohibitive, and have a profile of negative side effects, including serious drug-drug interactions, cardiac effects, and abdominal issues—including nausea, cramping, bowel urgency, and foul-smelling steatorrhea in many patients (Bersoux et al., 2017).

[1]Department of Surgery, University of Minnesota, MN, USA

[2]Preclinical Research Center, Department of Surgery, University of Minnesota, 295 Animal Science/Veterinary Medicine Building, 1988 Fitch Avenue, St. Paul, MN 55108, USA

[3]Schulze Diabetes Institute, Department of Surgery, University of Minnesota, MN, USA

[4]BioTechnology Institute, University of Minnesota, MN, USA

[5]Lead contact

*Correspondence: graha066@umn.edu (M.L.G.), sramacha@umn.edu (S.R.), ikram001@umn.edu (S.I.)

https://doi.org/10.1016/j.isci.2021.103421

For patients with class II obesity or higher (BMI $\geq$ 40 kg/m^2 or $\geq$ 35 kg/m^2 with comorbidities), bariatric surgery represents the gold standard therapy not only for weight reduction, but more importantly for control of cardiometabolic risk factors (Ikramuddin et al., 2013). A 30% total body weight loss in the first year is common following most bariatric surgeries, with greater weight loss seen in patients with higher BMIs (Arterburn et al., 2018). In clinical studies, compared to intensive medical therapy, bariatric surgery is not only associated with greater weight loss but also improved the control of T2D, other cardiometabolic risk factors, and mortality (Carlsson et al., 2020; Ikramuddin et al., 2013; Reges et al., 2018; Schauer et al., 2014). Of the two most common procedures, Roux-en-Y gastric bypass (RYGB) and VSG, RYGB was historically thought to result in better metabolic improvements, yet recent studies have shown quite similar metabolic outcomes between RYGB and VSG (Arterburn and Gupta, 2018). VSG also has an increased safety profile through the avoidance of gastrointestinal rearrangement including decreased perioperative mortality, decreased length of hospital stay, and decreased long-term postoperative complications such as micro- and macro-nutrient deficiencies, and thus VSG has emerged as the most common procedure performed (Arterburn and Gupta, 2018; Arterburn et al., 2018; Ikramuddin, 2015; Johnson et al., 2019). T2D remission associated with bariatric surgery often precedes significant weight loss and can persist despite weight regain, suggesting metabolic benefits stem from mechanisms more complex than simply a reduction in weight (Arterburn and Gupta, 2018). Although bariatric surgery provides remarkable clinical benefit, efficacy can decrease over time, especially in patients with the most pronounced preoperative metabolic dysfunction (Arterburn and Gupta, 2018; Arterburn et al., 2018; Shah and Laferrère, 2017), reflecting the gap in understanding of what factors promote the best metabolic response, as well as the identification of adjunctive therapies that improve the durability of the response to VSG.

Despite more than a decade of research that has uncovered the metabolic benefits of bariatric surgery, the underlying mechanisms and specific contributions of complex integrated physiologic systems to metabolic changes remain incompletely understood (Batterham and Cummings, 2016). In MUO, T2D develops owing to increased peripheral and hepatic insulin resistance (IR). A key driver of IR is adipose tissue (AT) inflammation, with local inflammation specifically in the VAT contributing to the development of T2D, the MetS, and poor outcomes in the MUO (Longo et al., 2019). Macrophages are major drivers of the development and control of VAT inflammation, with the histologic hallmark of AT inflammation being macrophages surrounding dead or dying adipocytes in crown-like structures (CLSs) (Panduro et al., 2016; Shapouri-Moghaddam et al., 2018; Wang et al., 2019). Classically macrophages have been described in a paradigm of polarization between M2 (anti-inflammatory) versus M1 (pro-inflammatory), though further subsets on the spectrum of macrophage function are being increasingly appreciated (Shapouri-Moghaddam et al., 2018). In VAT, M2-like macrophages work bidirectionally with tissue-resident regulatory T cells, which are also critical in the control of VAT inflammation and IR (Panduro et al., 2016). VAT Tregs have a unique phenotype including distinct antigen-specific receptors and increased anti-inflammatory cytokine production (Panduro et al., 2016). In mouse models of obesity, there is a dramatic increase in CLSs and reduction in VAT Tregs associated with VAT inflammation and IR, while in lean mice VAT is enriched with M2-like macrophages as well as Tregs (Becker et al., 2017; Panduro et al., 2016). Additionally, the gut microbiome has long been described as altered in obesity and the MetS, with the most recognized example being an imbalance in the *Firmicutes/Bacteroidetes* ratio (Ley et al., 2005, 2006; Turnbaugh et al., 2009). Microbially produced metabolites have the capacity to alter immunocyte phenotypes, such as bile acids (BAs) controlling Treg differentiation (Hang et al., 2019). This suggests crosstalk between the microbiome, metabolome, and immune system is central to the regulation of VAT inflammation and systemic metabolic health.

Research into these interconnected systems that contribute to metabolic changes during treatment for obesity in humans is fraught with challenges. The ability to perform repeated sampling is limited, especially of deep compartments like the omentum or portal venous system. Adherence to diet control, exercise programs, and medications is poor even in human subjects participating in clinical trials, which can lead to spurious conclusions. Additionally, the extensive clinical variability in patients undergoing bariatric surgery makes both baseline and longitudinal assessments difficult. Many patients lose significant weight in preparation for surgery or are on medications such as metformin, which can drastically alter both individual and systemic factors that contribute to treatment outcomes including the microbiome, metabolome, gastrointestinal hormones, immune system, and nervous system (Batterham and Cummings, 2016; Vujkovic-Cvijin et al., 2020). Only a fraction of these confounders can be standardized and controlled for clinically, and some are unable to even be reliably observed and measured. This highlights the need for nonclinical models capable of mimicking the complexity of the clinical situation to understand mechanisms that are

poorly understood in patients in the clinical setting (i.e., reverse translation) or evaluate promising obesity interventions (i.e., forward translation).

Animal models have been leveraged to address many of these challenges by allowing for the control of environmental factors, treatment compliance, and utilizing genetically modified animals. Animal models of obesity and T2D are primarily carried out in rodents and occasionally large animals, and rely heavily on genetic susceptibility/alteration or dietary induction. Models of bariatric surgery in rodents have shown some promise, but have been limited owing to high surgical stress and mortality (17% mortality for VSG), need for microsurgical proficiency, as well as profound differences in surgical approach and gastrointestinal anatomy (Rao et al., 2010; Stevenson et al., 2019). Although rodent models have resulted in vast leaps in our understanding of obesity and T2D, translation of therapeutic interventions for obesity to human patients has been disappointing. Preclinical studies often overestimate treatment effects or fail to identify adverse effects (Vickers et al., 2011), as has been demonstrated with leptin as a treatment for obesity. Although leptin administration in deficient mice reverses obesity and IR (Halaas et al., 1997), it has only been effective in patients with congenital deficiency or lipodystrophy and has been ineffective in translation to the general obese population (Zhao et al., 2020). This suggests integrative biology is fundamentally different between lower-order species like inbred mice and animals with increased complexity, highlighting the need for a translational model that can account for the cross-talk between many interconnected biologic systems while still controlling for confounding factors (Blüher and Mantzoros, 2015; Chou and Perry, 2013).

Our goal was to reverse translate the VSG model in nonhuman primates (NHPs), mimicking the diversity and spectrum of obesity and metabolic health in clinical patients, to assess the validity of this biologically complex model of obesity intervention. We utilized a highly translational animal, the macaque, with strong construct and face validity, while leveraging advantages of an animal model that cannot be performed in humans such as repeated sampling, dietary, and environmental control, and a sham surgical group. The translatability of this model is strengthened by the use of cooperative handling of the NHPs which results in less stress- and sedation-induced metabolic and immunologic perturbations often introduced by conventional handling techniques (Graham et al., 2012; Graham and Schuurman, 2015; Hocum Stone et al., 2021). This model utilizes VSG, the most common treatment for obesity and the MetS (Ikramuddin et al., 2013), to affect multiple interrelated biologic systems and address construct, face, and predictive model validity, thus bridging the gap between rodents and humans in anatomy, behavior, BA and microbiome diversity, and immunology.

We demonstrate that VSG induces weight loss, sustained metabolic control, and BA upregulation in NHPs that is predictive of outcomes in humans, both recapitulating the hallmarks of the disease and also responding similarly to treatment (Belzung and Lemoine, 2011; Willner, 1984). We also report that VSG in NHPs results in significant differences in weight and metabolic status occurring independent of caloric intake, and induces a long-term shift toward reduced inflammation in the VAT of NHPs. Our exploratory findings, which focused on the early immunologic changes after VSG, showed polarization of VAT immunocytes toward a regulatory phenotype with greater potency and activation. We specifically demonstrate an increase in classic anti-inflammatory M2 macrophages and Tregs as well as a spectrum of regulatory myeloid and Treg subpopulations in the AT microenvironment. These findings in the NHP model serve as a translational bridge between rodent and human studies of the mechanisms underlying metabolic, physiologic, and immunologic changes induced by bariatric surgery and allow for the creation of more effective therapies for the treatment of obesity and T2D.

RESULTS

Baseline characteristics

Animals were paired according to baseline weight, body condition score (BCS), and fasting c-peptide levels, and randomized to sham surgery or VSG (n = 3 per group). There were no significant differences in baseline characteristics between the VSG and sham groups (Table S1). At baseline while being fed a typical primate diet with high protein and low fat, all animals were spontaneously obese (average weight 13.4 $\pm$ 0.7 kg) with a fasting glucose of 62.1 $\pm$ 4.2 mg/dL, normal hemoglobin A1c (HgbA1c) of 4.3 $\pm$ 0.2%, and normal fasting C-peptide of 4.6 $\pm$ 0.6 ng/mL.

VAT was assessed at baseline and at one year postoperatively for immune markers of chronic AT inflammation that is seen in obesity such as CLSs (Figure 1J) – macrophages surrounding dead adipocytes. The AT morphometry of NHPs (Figure 1K) was similar to humans.

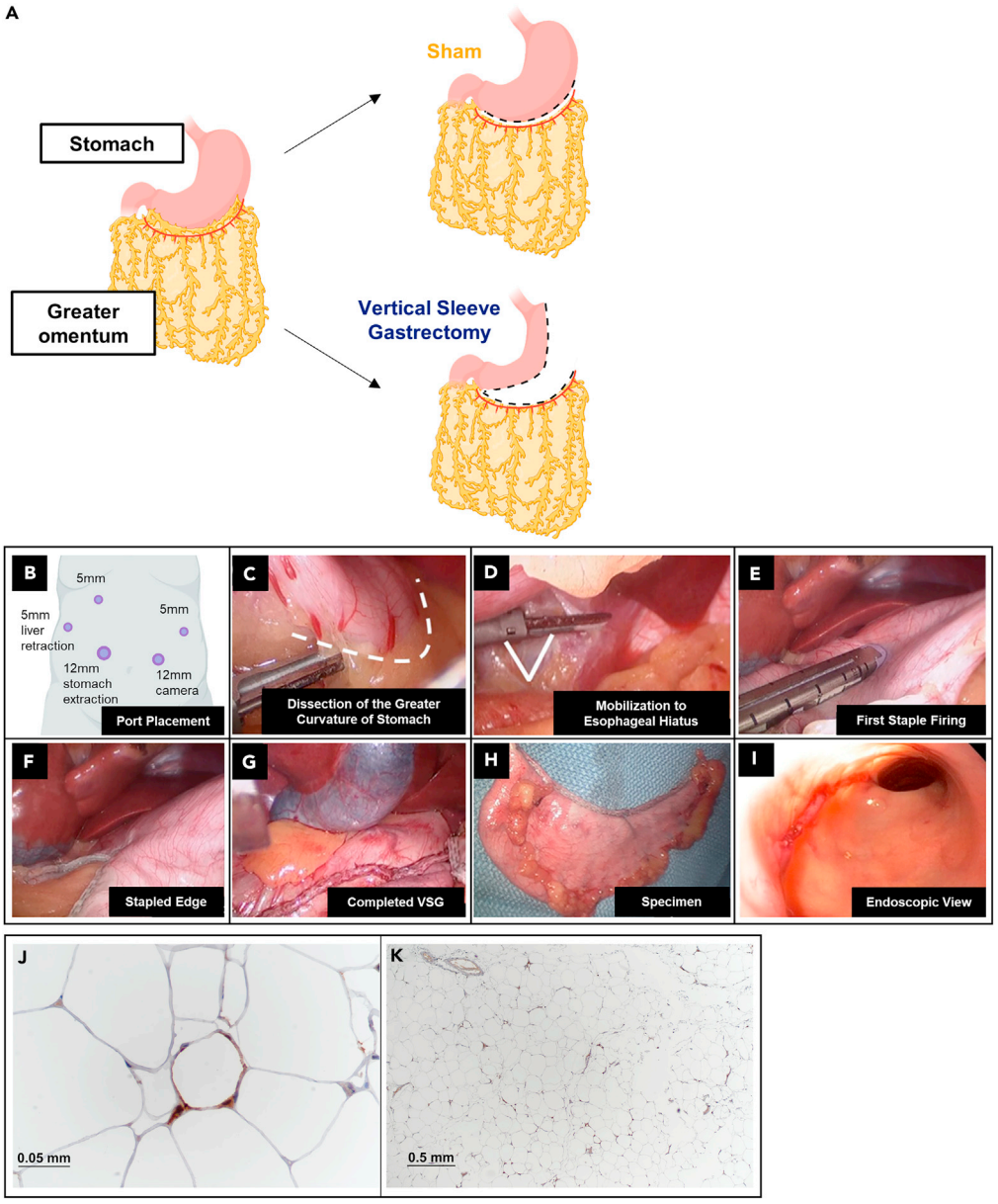

Figure 1. Surgical approach and intraoperative photographs of sham surgery and VSG in the NHP

(A–G) VSG was performed laparoscopically in the usual fashion (A), while sham surgery replicated surgical stress without anatomic alterations (A). Port placement was the same as in humans (B), and dissection occurred along the greater curvature of the stomach with the division of the short gastric arteries (C). Sham surgery was concluded without stomach stapling, while VSG proceeded with mobilization of the esophageal hiatus (D) and stapled sleeve gastrectomy (E–G).

(H) Removed stomach specimen.

(I–K) (I) Endoscopic view with intact staple line. At baseline, CLSs of macrophage inflammation in AT were observed (J, representative image, IBA-1 stain, 40x magnification, scale bar = 0.05 mm). AT morphology was homologous to humans (K) (representative image, IBA-1 stain, 4x magnification, scale bar = 0.5 mm).

See also Figure S12.

Surgical technique, morbidity, and mortality

The sham procedure replicated the surgical stress associated with VSG without anatomic alteration, and involved dissection along the greater curvature of the stomach with takedown of the omentum (along the dotted line, Figure 1A) and division of the short gastric arteries. Figures 1B–1I demonstrate the intraoperative steps of the laparoscopic VSG that were identical to the operation as it is performed in humans.

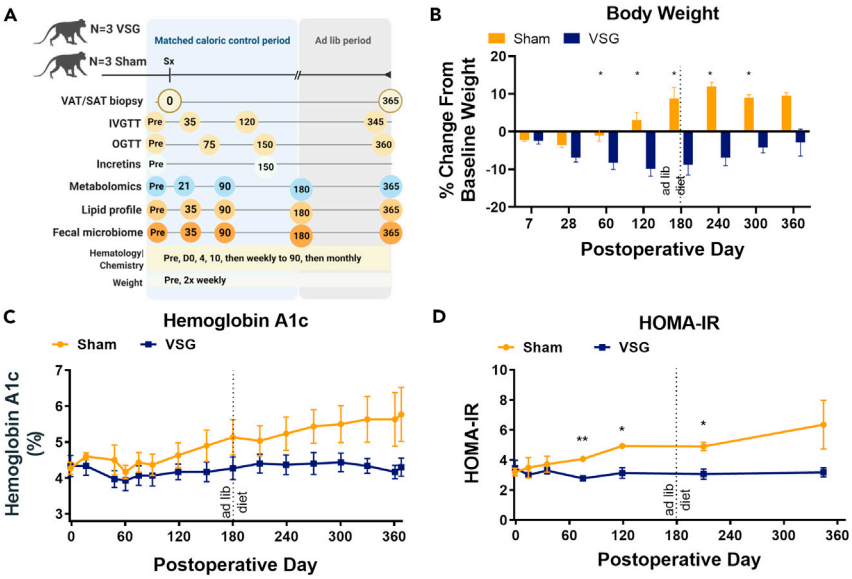

Figure 2. Weight loss, feeding patterns, and glucose metabolism one year after VSG in NHPs

(A) Study design schematic of the long-term study. (B–D) VSG resulted in weight loss (B) even with equivalent caloric intake postoperatively. When allowed to eat to caloric excess after D180, VSG animals' body weights increased slightly but still remained at a net negative weight from baseline (B). One animal in the sham group did become hyperglycemic and thus lost weight, and as such was excluded from the calculations in (B). Metabolic control as measured by HgbA1c (C) and HOMA-IR (D) was stable for animals who underwent VSG throughout the study year, even with weight regain by the VSG cohort after D180. *$p < 0.05$, **$p < 0.005$, sham vs. VSG. Data reported as group average ±SEM.
See also Figures S1, S2, S4, S10, and S11 and Tables S2, S3, and S7.

The only postoperative morbidity during the long-term study was a small, asymptomatic, easily reducible port site hernia in one animal on routine body condition score (BCS) exam 90 days postoperatively (D90). All animals survived planned experimental follow-up to one year.

In the short-term, exploratory study to 28 days postoperatively focusing on immunocyte changes, one animal developed sepsis starting on D3 based on clinical observation and laboratory values, and was euthanized on D6. The animal was found to have a leak from the staple line, and as such was excluded from any postoperative analyses owing to this technical complication.

Weight loss and feeding patterns

In the immediate postoperative period of the long-term study, up to day 180 postoperatively, animals in both groups were given a matched caloric offering (Figure 2A). During the immediate postoperative period, animals undergoing sham surgery and VSG lost 5.5 ± 0.8% of their initial body weight (Figure 2B). By D60, the weight trajectories significantly diverged (Figure 2B); the sham cohort started regaining, while the VSG group continued to lose weight. The sham cohort returned to their baseline preoperative weight by D70 with subsequent continued weight gain; in contrast, the VSG cohort lost 8.9 ± 2.2% of their preoperative weight while receiving a matched caloric offering.

The VSG group maintained this significant weight loss, while the sham group had gained 8.6 ± 1.5% (absolute difference 17.5%) at six months, at which time animals moved into the cross-over phase of *ad libitum* access to excess calories for the remainder of follow-up. Prior to the start of *ad libitum* caloric access, the sham and VSG groups had matched caloric offerings, and calculated caloric intake, which was inclusive of supplemented foods, was similar (Figure S2, approximately 40 kcal/kg/day).

The maximum percent weight loss difference between the groups was observed on D240, with an absolute difference of 18.9% between the groups. The maximum weight lost was −14.4% from baseline by Animal E after VSG (Figure S1E; for the VSG group overall −10.3 ± 2.3%, Figure 2B) at D90. At D365, the sham group exhibited 8.1 ± 1.1% weight gain compared to preoperative. During later timepoints, individual animals

began to drive the trend in these small (n = 3) groups; one animal in the sham cohort developed hyperglycemia and began to lose weight while the others maintained their weights (Figures S1A–S1C). After *ad libitum* feeding, the caloric intake did not differ significantly between groups (Figure S2). With increasing access to calories, animals in the VSG group were able to regain weight to near baseline, with 2.9 ± 4.3% weight loss compared to preoperative weight at D365 (increase of 7.4% from nadir weight loss). In the sham group, a single animal developed overt hyperglycemia and weights collected during this period was excluded, to account for the hyperglycemia-induced weight loss of that specific animal. Individual animal weight curves and caloric intake are available as Supplemental Data (Figures S1 and S2), full details of changes in BCS, umbilical circumference, and weight are available as Supplemental Data (Table S2). BMI equivalent was calculated as body weight (kg) divided by the square of crown-to-rump length (cm) (Jen et al., 1985). Congruent with reduced adiposity, VAT adipocyte volume was maintained in the obese sham animals at D365 but was statistically significantly reduced after VSG (Figure S3, 11.2 ± 0.8 × 10^4 μm^3 at D365 vs. 16.2 ± 1.3 × 10^4 μm^3 at D0, p = 0.03).

Changes in glucose metabolism

At baseline, all animals in the long-term study were nondiabetic with fasting glucose of 62.1 ± 4.2 mg/dL and HgbA1c 4.3% ± 0.2% (Table S1). There was a trend toward increased glucose utilization ($K_{glucose}$) in the VSG compared to the sham group at baseline (Figure S4A). At the end of the study period (D365), HgbA1c increased to 5.8 ± 0.8% in the sham group and remained stable at 4.3 ± 0.3% in the VSG group (Figure 2C). This was further demonstrated by Homeostatic Model Assessment for insulin resistance (HOMA-IR) levels increasing over time in the sham group, while remaining stable in the VSG group; this difference reached statistical significance at D75 (Figure 2D, 4.1 ± 0.1 for sham vs. 2.8 ± 0.2 for VSG, p = 0.004). Further metabolic characterization is shown in Figure S4. Intravenous glucose tolerance testing (IVGTT) performed longitudinally showed that VSG animals displayed stable glucose handling, while sham animals had an impaired glucose disposal rate during IVGTT (Figure S4A, $K_{glucose}$, 0.9 ± 0.5 for sham vs. 4.3 ± 1.1 for VSG, p = 0.05). By D345, fasting glucose was elevated in the sham group compared to the VSG group (Figure S4C, 108.1 ± 19.1 vs. 52.1 ± 4.7 mg/dL, p = 0.05). Postprandial glucose levels as measured by oral glucose tolerance testing (OGTT) were also slightly elevated in sham animals at D150, and markedly impaired at D360 (Figure S4D), while postprandial glucose levels remained relatively stable in animals who underwent VSG. Over time, fasting c-peptide increased substantially in the sham group, increasing to 173% of baseline by D120 and 191% of baseline by D345, with no change in the VSG group (Figure S4B), suggesting the impaired glucose disposal in the sham group was related to peripheral IR rather than impaired production. Full details of pre and postoperative metabolic characteristics are available as Supplementary Data (Table S3).

Alterations in adipose tissue immunocytes

VAT macrophage phenotypes were assessed in the long-term study by flow cytometry one year after sham surgery or VSG. Macrophages (defined as $CD64^+CD45^+$ stromal vascular fraction [SVF] cells) expressed less CD206 after VSG, suggesting a reduction in the tissue-resident macrophage population (Figure 3A, sham 26.0 ± 4.1% vs. VSG 11.7 ± 1.3%, p = 0.03). Additionally, these tissue-resident macrophages had significantly reduced expression of activation markers CD11c, HLA-DR, and CD169 (Figure 3B; $CD11c^+$: sham 32.6 ± 4.4% vs. VSG 13.5 ± 5%, p = 0.02; $HLA\text{-}DR^+$: sham 91.8 ± 4.1% vs. VSG 62.3 ± 3.9%, p = 0.006; $CD169^+$: sham 63.4 ± 7.1% vs. VSG 33.7 ± 3.8%, p = 0.02).

CLS density was quantified by counting macrophages surrounding adipocytes in the classic CLS morphometry in VAT and subcutaneous adipose tissue (SAT) from D0 and D365. SAT CLS density was increased after both surgeries (p < 0.05 sham; p = 0.05 VSG) (Figure 3D), while in VAT, VSG but not sham resulted in a significant reduction in CLS density (Figure 3C; VSG -4.0 ± 1.0 Δchange from D0, p = 0.02 D0 vs. D365; p = 0.06 sham vs. VSG at D365) suggesting reduced VAT inflammation. Similar trends were seen in CD3-stained cells (Figures 3E and 3F). In VAT, $CD3^+$ cells were significantly reduced −1.7 ± 0.6 after VSG (p = 0.05 D0 vs. D365) yet increased 2.8 ± 3.3 after sham surgery, and in SAT $CD3^+$ cells were increased after both sham surgery and VSG.

Microbiome and metabolite changes

We assessed the fecal microbiome longitudinally for the long-term study (Figure S5). A lower *Firmicutes:-Bacteroidetes* ratio, often associated with a lean phenotype, was seen up to D90 after VSG but not after sham surgery, even though animals had equivalent caloric intake (D35: sham 10.4 ± 5.1, VSG 1.1 ± 0.4,

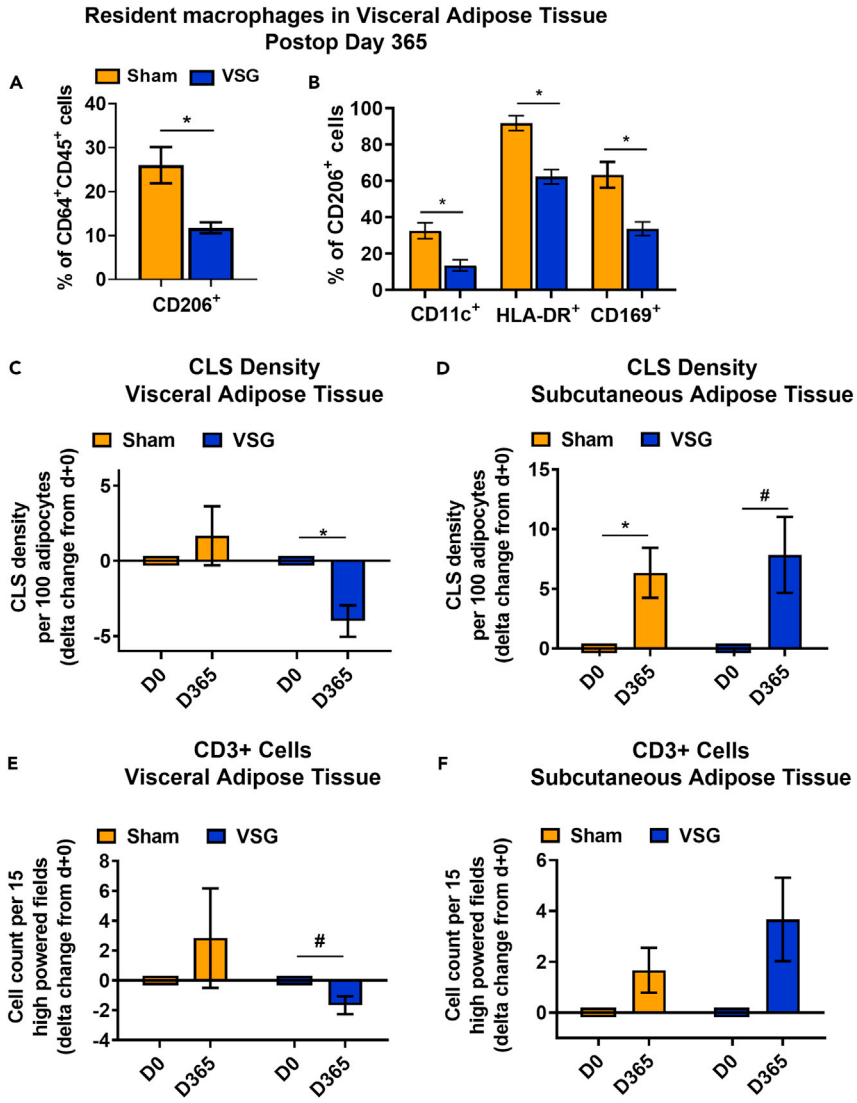

Figure 3. Macrophage phenotypes, CLSs, and T cell infiltration in AT one year after VSG

(A and B) Tissue-resident macrophages ($CD64^+CD45^+$ stromal vascular cells) in VAT were significantly suppressed after VSG (n = 3) compared to sham (n = 3) (A), with less CD206 expression (a classic M2 macrophage marker) and less expression of activation markers CD11c, HLA-DR, and CD169 (B).

(C–F) (C) CLS density (expressed as Δchange from D0) trended to slightly increased after sham surgery, but was significantly reduced in VAT after VSG suggested reduced inflammation in the VAT. This was VAT-compartment specific, with SAT (D) demonstrating increases in CLSs after both sham surgery and VSG. Similar trends were seen with $CD3^+$ T cells, with a decrease after VSG in VAT (E) but not SAT (F). *p < 0.05, sham vs. VSG; #p = 0.05, sham vs. VSG. Data reported as group average ±SEM.

See also Figure S3.

p = 0.14 sham vs. VSG; D90: sham 22.2 ± 19.1, VSG 2.0 ± 0.3, p = 0.25 sham vs. VSG). After D180, there were no differences in the *Firmicutes:Bacteroidetes* ratio between sham and VSG groups. The fecal microbiome for each individual animal (Figure S6) demonstrates the wide inter-animal diversity at the bacteria species level. Changes in bacterial abundance were observed postoperatively, but with a different pattern depending on the bacterial species, and were not specifically associated with VSG or sham. *Subdoligranulum spp.* (Figure S6, light blue bars) was one of the largest populations seen, and generally increased after surgery. In animals B (sham), D (VSG), and F (VSG), *Prevotella copri* (Figure S6, salmon bars) overall appeared to decrease after surgery.

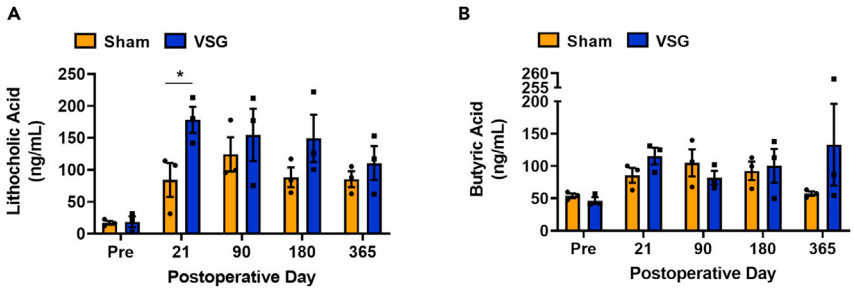

Figure 4. Peripheral serum metabolite changes after VSG

(A) The secondary BA lithocholic acid was significantly increased after VSG compared to sham at D21 and equalized by D90.

(B) The SCFA butyric acid trended toward increased at D21 after VSG. *p < 0.05 sham vs. VSG. Data reported as group average ±SEM.

See also Figures S5, S6, and Table S4.

The peripheral serum metabolome was evaluated by shotgun/untargeted metabolomics up to D90 to assess a wide variety of metabolites, and subsequently with targeted/quantitative metabolomics of specific metabolites of interest. Table S4A demonstrates the heterogeneity, complexity, and breadth of BAs found in the NHP serum by targeted metabolomics similar to humans. Both primary and secondary BAs were increased at D21 after surgery in VSG compared to sham, with secondary BAs showing the greatest fold-increases and many reaching or approaching statistical significance (Table S4A). Primary BAs decreased at D90 after VSG, and by D365 were mildly elevated again, though with a fold change of only approximately 2-fold over sham without much statistical significance (Table S4A). Lithocholic acid, a metabolite of interest owing to its immunomodulatory effects, was statistically significantly increased after VSG compared to sham surgery at D21 (Figure 4A, sham: 84.1 ± 26.4 ng/mL, VSG 178.3 ± 20.5 ng/mL, p = 0.048) but equalized at later timepoints. Short-chain fatty acids (SCFAs) also trended toward increased after VSG in comparison to sham surgery (Table S4B). Butyric acid, an important SCFA made as a byproduct of metabolism by colonic bacteria and thought to have anti-inflammatory effects, was not different between groups (Figure 4B).

Phenotypic profiling and diversity of myeloid and lymphoid immunocytes by mass cytometry

To explore the impact of VSG on AT immunocytes, we performed a short-term, exploratory study (Figure 5A) in a group of animals that exhibited matched weight loss under identical surgical conditions as the cohort in the long-term study (Figure 5B). We employed a 36-antibody CyTOF (time of flight mass cytometry) panel developed and validated for use in macaques to assess the frequency dynamics and phenotypic diversity of myeloid and lymphoid immunocytes across AT compartments. In the peripheral circulation, we observed an increase in the ratio of M2/M1 macrophages immediately post-VSG that reached its peak on D21. The ratio of M2/M1 macrophages was increased in VAT following VSG, with an over 6-fold increase in VAT compared to a 1.5-fold increase in SAT, and returning to baseline levels in peripheral blood lymphocytes (PBLs) at D28 (Figure 5C). Analysis of the kinetics of Treg expansion in the peripheral circulation showed that there was an increase in the frequency of Tregs that mirrors the conversion to M2 macrophages. Similarly, VSG induced a ~2-fold increase in Tregs in VAT and SAT and a 3-fold increase in PBLs on D28 (Figure 5D). Following VSG, Tr1 cells increased 2-fold increase in VAT and SAT with no change in PBLs (Figure S8A), as well as a reduction in proliferating Ki67 + CD4+ T cells in both VAT and SAT (Figure S8B), though none of these changes are significant. Though we could not establish a direct correlation between these populations because of our small exploratory sample size, the kinetics of our observations suggest that the establishment of an anti-inflammatory microenvironment by M2 macrophages might promote the expansion of the regulatory T cells, especially Tregs and Tr1s.

To visualize complex myeloid cell phenotypes in these three tissue compartments, we performed unsupervised clustering analysis on myeloid cells from these compartments before and after VSG. Twelve distinct cellular populations within myeloid cells were identified by the tSNE and FlowSOM clustering analysis based on the median expression profile of the 29 myeloid lineage markers (Figure S7). The distribution and cluster size of these FlowSOM populations are displayed on the tSNE map (Figure 5E) and summarized with bar plots for each compartment (Figure 5F), showing a substantial change in a relative frequency of populations 1, 2, 3, 9,

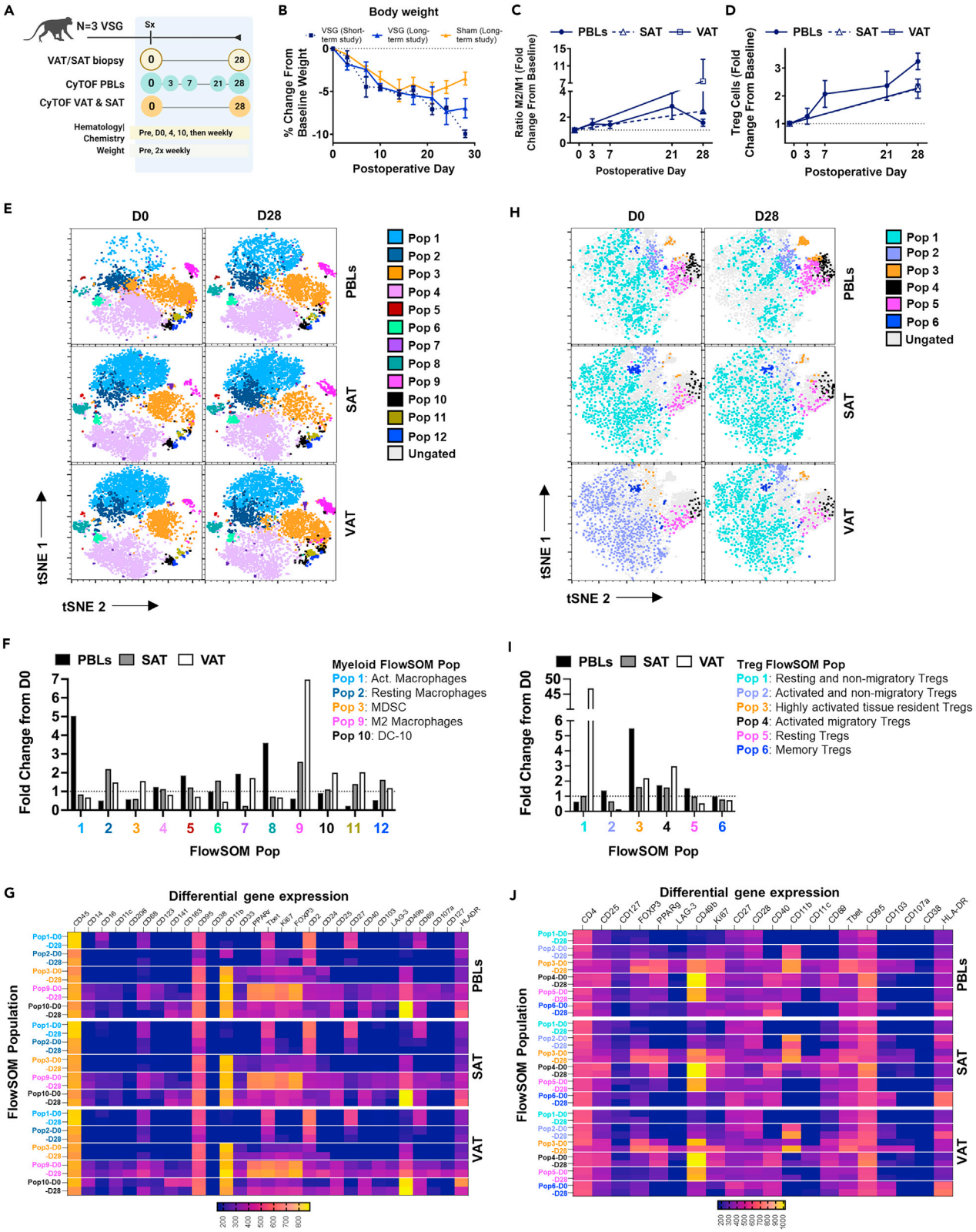
A
N=3 VSG
Sx
VAT/SAT biopsy
CyTOF PBLs
CyTOF VAT & SAT
Hematology| Chemistry
Weight
Pre, D0, 4, 10, then weekly
Pre, 2x weekly
B
Body weight
VSG (Short-term study)
VSG (Long-term study)
Sham (Long-term study)
% Change From Baseline Weight
Postoperative Day
C
PBLs SAT VAT
Ratio M2/M1 (Fold Change From Baseline)
Postoperative Day
D
PBLs SAT VAT
Treg Cells (Fold Change From Baseline)
Postoperative Day
E
D0
D28
PBLs
SAT
VAT
tSNE 1
tSNE 2
Pop 1
Pop 2
Pop 3
Pop 4
Pop 5
Pop 6
Pop 7
Pop 8
Pop 9
Pop 10
Pop 11
Pop 12
Ungated
H
D0
D28
PBLs
SAT
VAT
tSNE 1
tSNE 2
Pop 1
Pop 2
Pop 3
Pop 4
Pop 5
Pop 6
Ungated
F
PBLs SAT VAT
Fold Change from D0
FlowSOM Pop
Myeloid FlowSOM Pop
Pop 1: Act. Macrophages
Pop 2: Resting Macrophages
Pop 3: MDSC
Pop 9: M2 Macrophages
Pop 10: DC-10
I
PBLs SAT VAT
Fold Change from D0
FlowSOM Pop
Treg FlowSOM Pop
Pop 1: Resting and non-migratory Tregs
Pop 2: Activated and non-migratory Tregs
Pop 3: Highly activated tissue resident Tregs
Pop 4: Activated migratory Tregs
Pop 5: Resting Tregs
Pop 6: Memory Tregs
G
Differential gene expression
CD45 CD14 CD16 CD11c CD206 CD68 CD123 CD141 CD163 CD95 CD39 CD11b CD33 PPARg Tbet KI67 FOXP3 CD2 CD24 CD25 CD27 CD40 CD103 LAG-3 CD49b CD69 CD107a CD127 HLA-DR
FlowSOM Population
PBLs
SAT
VAT
J
Differential gene expression
CD4 CD25 CD127 FOXP3 PPARg LAG-3 CD49b KI67 CD27 CD28 CD40 CD11b CD11c CD69 Tbet CD95 CD103 CD107a CD38 HLA-DR
FlowSOM Population
PBLs
SAT
VAT

Figure 5. Diversity of myeloid and lymphoid immune cells one month after VSG

(A–C) Our short-term study (A) was designed to characterize early immunocyte changes in a group of animals with matched weight loss following VSG to the long-term study (B). VSG promoted M2-like macrophage polarization, increased the number of regulatory T cells, and decreased the number of proliferating T cells in the adipose tissue. Fold-change from baseline in PBLs, SAT, and VAT in the ratio of: (C) M2/M1 macrophages (M1: $CD206^{+}CD11c^{+}$, M2: $CD206^{+}CD11c^{-}$ of $CD14^{+}CD68^{+}CD3^{-}$ lym), M2/M1 in SAT n = 1, all others n = 2.

(D) Tregs ($FoxP3^{+}CD4^{+}$ of $CD3^{+}$ lym).

(E) *t*-SNE projection of 26,400 myeloid cells ($CD3^{-}CD20^{-}/CD45^{+}$ lym) sampled equally from PBLs (n = 2), SAT (n = 2), and VAT (n = 2) at D0 and D28 after VSG.

(F) 12 individual FlowSOM-identified myeloid populations from the *t*-SNE projection in (E) as fold change from D0.

(G) Heatmap showing mean expression of indicated markers across the 12 FlowSOM myeloid populations.

(H) *t*-SNE projection of 4860 Tregs ($CD25^{+}CD127^{-}/CD4^{+}$ lym) sampled equally from PBLs (n = 2), SAT (n = 2), and VAT (n = 2) at D0 and D28 after VSG.

(I) Six individual FlowSOM-identified Treg populations from the *t*-SNE projects in (H) as fold change from D0.

(J) Heatmap showing mean expression of indicated markers across the six FlowSOM Treg populations. Data reported as group average ±SEM.

See also Figures S7, S8, and S9, and Tables S5 and S6.

and 10 after VSG at D28 (Figure S9E, Table S5). Based on the expression intensity of canonical lineage markers (Figure 5G), populations 1 and 2 identify the activated ($Tbet^{hi}$, $CD69^{hi}$, $HLA\text{-}DR^{+}/CD11c^{+}CD68^{+}$) and resting ($Tbet^{low}$, $CD69^{-}$, $HLA^{-}DR^{+}/CD11c^{+}CD68^{+}$) macrophages, respectively. In Figure 5F, activated macrophages (population 1) were decreased in VAT and SAT after VSG, while resting macrophages were increased in VAT and SAT. In VAT, we observed a substantial increase in myeloid-derived suppressor cells (MDSC; population 3: $CD11b^{+}CD33^{+}HLA\text{-}DR^{low}/CD14^{+}CD68^{+}$, ~1.5-fold over baseline), anti-inflammatory macrophages (population 9: $CD11c^{-}CD206^{+}PPAR\gamma^{hi}/CD14^{+}CD68^{+}$, ~7-fold over baseline; PPARγ = peroxisome proliferator-activated receptor gamma), and tolerogenic dendritic cell (DC)-10 cells (population 10: $CD141^{+}CD163^{hi}/CD14^{+}CD11c^{+}$, 2-fold over baseline) (Figures 5F and 5G). Interestingly, in SAT we also observed a 2.6-fold increase in anti-inflammatory macrophages (population 9) after VSG (Figures 5F and 5G).

To dissect the phenotypic heterogeneity of Tregs ($CD25^{+}CD127^{-}/CD4^{+}$), we performed unsupervised clustering analysis using the tSNE and FlowSOM algorithms. We identified six unique populations of Tregs distinguished by the expression of canonical lineage markers and visualized the results using t-SNE (Figures 5H and S9) and bar plots for each compartment (Figure 5I). Based on the median intensity expression of each marker in Figure 5J, three clusters identified as resting and non-migratory (population 1), highly activated tissue-resident (population 3), and activated migratory (population 4) Tregs were substantially increased in VAT (~47, 2.1, and 2.9-fold over baseline, respectively) along with SAT (1.1, 1.6, and 1.6-fold over baseline, respectively) after VSG (Figures 5I and S9F, Table S6). Populations 2, 5, and 6 were identified as activated non-migratory, resting, and memory Tregs and remained unchanged in PBLs and decreased in SAT and VAT after VSG (Figure 5I). Notably, in VAT, SAT, and PBLs, both highly activated tissue-resident Tregs (population 3) and activated migratory Tregs (population 4) were enriched with $FoxP3^{hi}$ $PPAR\gamma^{hi}$ co-expression and displayed highest intensities for CD11c, LAG-3, CD49b, and CD69, along with variable expression level of CD11b, CD103, CD107a, Tbet, and HLA-DR, suggesting VSG induced proliferation and expansion of highly activated tissue-resident Tregs after VSG. The phenotype of the heterogeneous subsets of myeloid and regulatory T cells in VAT at baseline is distinctly different at one month after VSG, highlighting the importance of unraveling the role VSG plays in modulating the immune response.

Postoperative laboratory parameters

In the long-term study, both VSG and sham animals had mild leukocytosis and decrease in albumin levels postoperatively which normalized by day 21, suggesting similar responses to surgical stress in the immediate postoperative period (Figure S10). Animals were not dyslipidemic at baseline (Figure S11). Low-density lipoprotein (LDL) did not appear differentially effected by VSG or sham surgery, while high-density lipoprotein (HDL) was increased compared to preoperative values in the VSG group (at D365: 50 ± 5.686 mg/dL, p = 0.32 for VSG D0 vs D365; 39 ± 6.5 mg/dL, p = 0.19 for sham D0 vs. D365), though there were no significant differences between sham and VSG. Triglyceride levels were lowered in the VSG animals by 1 month postoperative and persisted throughout the study year (at D365: 109.7 ± 27.3 mg/dL, p = 0.09 for VSG D0 vs. D365; 110.7 ± 29.6 mg/dL, p = 0.99 for sham D0 vs. D365). Pre and postoperative lipid profile characteristics are included as Supplementary Data (Table S7).

Changes in gut hormones and adipokines

Hormone and adipokine secretion curves were recorded during OGTT preoperatively and at D150 (Figure 6) in the long-term study. No significant differences were noted in preoperative hormone levels between the VSG and sham cohorts. Pancreatic polypeptide (PP) and peptide YY (PYY) secretion remained relatively stable in the

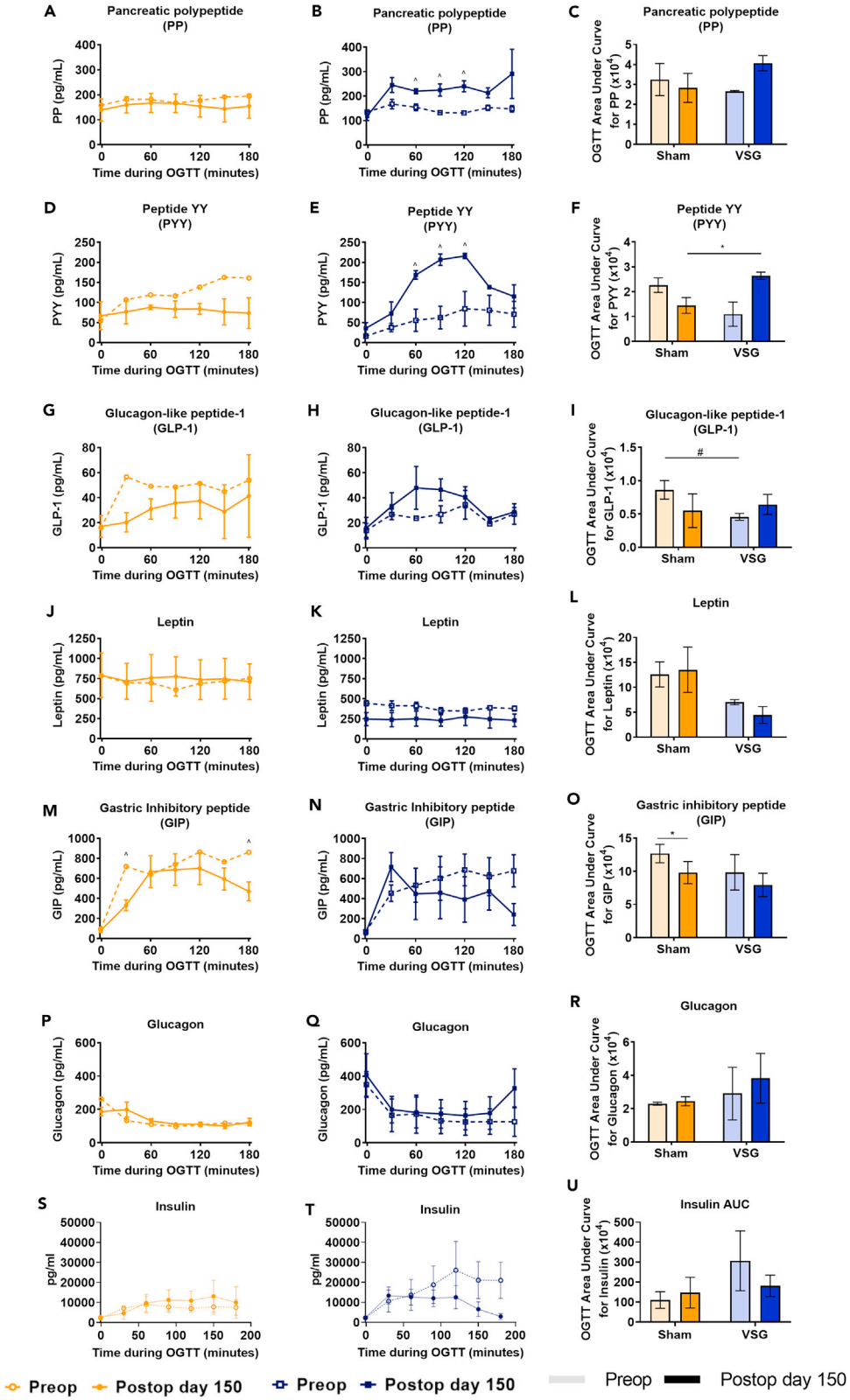
A
Pancreatic polypeptide (PP)
PP (pg/mL)
Time during OGTT (minutes)
B
Pancreatic polypeptide (PP)
PP (pg/mL)
Time during OGTT (minutes)
C
Pancreatic polypeptide (PP)
OGTT Area Under Curve for PP (x10^4)
Sham
VSG
D
Peptide YY (PYY)
PYY (pg/mL)
Time during OGTT (minutes)
E
Peptide YY (PYY)
PYY (pg/mL)
Time during OGTT (minutes)
F
Peptide YY (PYY)
OGTT Area Under Curve for PYY (x10^4)
Sham
VSG
G
Glucagon-like peptide-1 (GLP-1)
GLP-1 (pg/mL)
Time during OGTT (minutes)
H
Glucagon-like peptide-1 (GLP-1)
GLP-1 (pg/mL)
Time during OGTT (minutes)
I
Glucagon-like peptide-1 (GLP-1)
OGTT Area Under Curve for GLP-1 (x10^4)
Sham
VSG
J
Leptin
Leptin (pg/mL)
Time during OGTT (minutes)
K
Leptin
Leptin (pg/mL)
Time during OGTT (minutes)
L
Leptin
OGTT Area Under Curve for Leptin (x10^4)
Sham
VSG
M
Gastric Inhibitory peptide (GIP)
GIP (pg/mL)
Time during OGTT (minutes)
N
Gastric Inhibitory peptide (GIP)
GIP (pg/mL)
Time during OGTT (minutes)
O
Gastric inhibitory peptide (GIP)
OGTT Area Under Curve for GIP (x10^4)
Sham
VSG
P
Glucagon
Glucagon (pg/mL)
Time during OGTT (minutes)
Q
Glucagon
Glucagon (pg/mL)
Time during OGTT (minutes)
R
Glucagon
OGTT Area Under Curve for Glucagon (x10^4)
Sham
VSG
S
Insulin
pg/ml
Time during OGTT (minutes)
T
Insulin
pg/ml
Time during OGTT (minutes)
U
Insulin AUC
OGTT Area Under Curve for Insulin (x10^4)
Sham
VSG
Preop
Postop day 150
Preop
Postop day 150
Preop
Postop day 150

Figure 6. Serum incretins during OGTTs

(A–U) Major incretins in peripheral serum were measured via multiplex assay during OGTTs preoperatively and at D150. Pancreatic polypeptide (A–C) and peptide YY (D–F) were significantly increased and GLP-1 (total) (G–I) trended toward increased after VSG but not after sham surgery. Leptin (J–L), GIP (M–O), glucagon (P–R), and insulin (S–U) were not markedly changed by sham surgery or VSG. *$p < 0.05$, #$p = 0.05$, sham vs. VSG; ^$p < 0.05$, preop vs. D150. Data reported as group average ±SEM.

See also Table S8.

sham group while increasing after surgery in the VSG group (PP: Figures 6A–6C, PYY: Figures 6D–6F); comparing preoperative and postoperative areas under the curve of the OGTT demonstrated near statistically significant increases in both PP and PYY after VSG ($p = 0.07$ preop vs. postop PP, $p = 0.09$ preop vs. postop PYY). Additionally, at D150 after surgery, PYY levels were statistically significantly increased in the VSG cohort in comparison with sham ($p = 0.03$ sham vs. VSG). Total glucagon-like peptide 1 (GLP-1) secretion trended down in the sham cohort and increased in the VSG cohort (Figures 6G–6I, $p = 0.17$ sham preop vs. postop, $p = 0.45$ VSG preop vs. postop). Leptin trended toward a decrease after VSG (Figures 6J–6L, $p = 0.25$ VSG preop vs. postop). Gastric inhibitory peptide (GIP, Figures 6M–6O) secretion was significantly decreased in the sham cohort after surgery ($p = 0.03$ sham preop vs. postop). Glucagon (Figures 6P–6R) was not significantly affected by surgery. The VSG group had lower insulin levels during OGTT at D150 as compared to preoperatively (Figures 6S–6U), though these changes were not significant ($p = 0.45$ VSG preop vs. postop). Full pre and postoperative hormone and adipokine characteristics are included as Supplementary Data (Table S8).

DISCUSSION

In this study, we report a model of laparoscopic VSG performed in an NHP as an innovative translational approach to the understanding of obesity and its treatment. This model demonstrates strong preclinical validity in the three major categories of construct, face, and predictive validity (Eggel and Würbel, 2020; Willner, 1984), closely mimicking both the surgical approach and patient outcomes are seen clinically, including weight loss with reduction of adiposity, metabolic improvements, increased postprandial incretin secretion, gut microbiome changes, and increased BA levels. We also report weight-independent metabolic control and long-term reduction of inflammation in the VAT in NHPs after VSG. To explore this change in VAT inflammation after VSG, our short-term, exploratory study investigated the early immunologic changes one month after VSG, demonstrating the polarization of immunocytes in the VAT toward a regulatory phenotype with greater potency and activity of these regulatory cells. Taken together, our findings suggest bariatric surgery may regulate VAT inflammation to improve metabolic outcomes, as opposed to the conventional hypothesis that the benefits of surgery are primarily a result of weight loss alone. Additionally, these findings suggest that as early as one month postoperatively, VSG can modulate the VAT immune phenotype, disrupting the obesogenic memory of the VAT immune system, gleaning new insight into how we can optimize obesity treatments. Our preclinical model of VSG in the NHP will allow for a better understanding of the complex, interrelated systems impacted by bariatric surgery to improve the efficacy of treatment for patients with obesity and metabolic dysregulation.

On a controlled diet, weight diverged significantly between NHPs undergoing VSG that had a nadir weight loss of 14% during follow-up and an average weight loss of 9% at D180 with sustained metabolic control, while animals who underwent sham surgery had an average weight gain of 9% at D180 with worsening metabolic control. Historically, the efficacy of bariatric surgery in humans was attributed to its ability to induce caloric restriction and/or malabsorption (Buchwald, 2014). We equalized caloric intake between the sham and VSG animals up to D180 to investigate the effects of VSG independent of caloric intake—a question that cannot be assessed reliably in humans. Our study suggests that neither caloric restriction nor weight loss completely accounts for metabolic improvements after VSG. The equal weight loss between the two experimental groups up to D14 can be attributed to diet adjustments consistent with surgical manipulation of the gut and surgical stress, with leukocytosis, increased platelet count, and decreased albumin. However, because the sham surgery control group gained weight and had worsening metabolic control even with equal caloric intake to the VSG group, this revealed that the weight loss and metabolic control experienced by animals six months after VSG was not solely owing to surgical stress and postoperative caloric restriction. We demonstrate the dramatic and sustained weight loss and metabolic control exhibited after VSG was independent of caloric restriction up to D180, as animals who underwent sham surgery but with equivalent caloric intake gained weight and had worsening metabolic control. In the clinical situation, diet composition and caloric intake have presented as major confounding factors in untangling the relationship between weight and the MetS, and our model is able to effectively study this relationship in a way that is impossible in humans.

The magnitude of weight loss observed in our NHPs was less than in most clinical studies that report a weight loss of 25–30% after VSG, with several potential contributing factors. In the clinical setting, most patients undergoing bariatric surgery are consuming a very low or low-calorie diet, while the NHP cohort in this study did not. NHPs in this study developed spontaneous obesity without diet manipulation, a unique strength of our study as compared to small animal models of obesity that have relied on genetic manipulation or artificial diet alterations such as uniformly high fat or sucrose that are not encountered in the clinical setting (Kleinert et al., 2018; Yu, 2017). In future studies, exposing obese animals to a calorie-dense Western diet prior to entry may further improve the agreement in magnitude. Although the weight loss was more modest than the clinical situation, it is likely to be attributed to factors that can be tuned dependent on the target patient population of interest. The NHPs in this study were spontaneously obese but metabolically healthy, in comparison to the typical patient often reported in the literature that is morbidly obese and very metabolically unhealthy undergoing VSG. A BMI equivalent calculation in NHPs (Vaughan and Mattison, 2016) shows that our cohort, while obese, is a BMI ratio of approximately 1-1.5 fold higher than normal as opposed to the more severely elevated BMIs of patients, almost 2-fold higher than normal, who commonly undergo bariatric surgery (Ikramuddin and Livingston, 2013). Additionally, our cohort was free of metabolic comorbidities at enrollment, an MHO phenotype (Wu et al., 2012). Most clinical bariatric surgery studies report early (days to weeks) improvement in metabolic control in patients with MUO (Affinati et al., 2019) and we reveal a more gradual (weeks to months) change in metabolic function and more modest weight loss in MHO animals where VSG prevents the progression to MUO while sham animals develop MUO. Changes in weight and metabolic control were expected to be moderate given this baseline of our cohort, making these significant changes even more compelling as they can be further explored with a more severe phenotypic cohort. We also assessed cholesterol and lipid levels in our NHPs, as hyperlipidemia is a common component of the MetS, but overall saw very little change, with the exception of an increase in HDL in the VSG group postoperatively, while it remained stable in the sham group. These findings were not surprising given their preoperative metabolic health. Measuring hypertension was beyond the scope of the current study, though in the future could be assessed with cooperation or telemetry. We intentionally utilized modest animal numbers to explore the utility of the model and generate expected differences broadly capturing outcomes of interest to appropriately power future studies. We observed significant differences in weight loss and metabolic control (Tables S1, S2, and S3) after VSG in this approach, even with modest numbers suggesting the sensitivity of this model to assess these outcomes is robust. We anticipate that these differences will become even more pronounced by introducing factors such as Western diet, very low-calorie diet, increased BMI, or IR at enrollment dependent on the patient phenotype intended for modeling.

Six months after surgery, animals continued identical diets but with no restriction to quantity, after which sham animals continued to gain weight and demonstrate worsening metabolic control, to the extent that one animal became fully diabetic with subsequent weight loss. This model is uniquely well-suited for accurate assessment of metabolic parameters; the ability to perform clinically relevant oral and intravenous glucose tolerance testing with cooperative handling reduces the stress- and sedation-induced hyperglycemia ubiquitous in rodent studies (Graham, 2017; Graham et al., 2012; Hocum Stone et al., 2021). We deeply characterized the metabolic profile of our cohort with HgbA1c, HOMA-IR, glucose disposal, and c-peptide levels, demonstrating that the sham group had increased peripheral and hepatic IR which is indicative of the metabolic syndrome which may lead to diabetes that is seen in the MUO clinical scenario.

Surprisingly, when offered access to unlimited calories, both groups maintained similar caloric intake, with VSG animals consuming more calories per/kg than sham animals, but still maintained a net weight loss as compared to the sham group's weight gain postoperatively. This finding challenges the dogma of VSG as a solely restrictive therapy for obesity. Though these animals regained weight, they still had a net 2.9% weight loss from baseline at the study end, suggesting that even with caloric excess VSG is capable of promoting benefit. Although it is known that humans often regain weight after bariatric surgery, it is difficult to assess caloric intake in a controlled environment in humans owing to reporting bias (Mingrone et al., 2015). It has also been highly debated whether bariatric surgery induces weight-independent metabolic improvement, or if metabolic improvement is solely owing to weight loss (Affinati et al., 2019). The weight gain-independent metabolic control seen in our NHP model supports findings in humans and rodents that weight changes are not the only way that VSG improves metabolic parameters (Affinati et al., 2019; Frikke-Schmidt et al., 2017), and that more complex physiologic changes after VSG can confer long-term metabolic control independent of weight.

Gastrointestinal hormones, or incretins, are key players in the maintenance of hunger, satiety, and weight, and have been implicated in the efficacy of bariatric surgery in sustained weight loss and metabolic control

(Dimitriadis et al., 2017). We observed an increase in post-prandial PP and PYY VSG in comparison with sham surgery, which is similar to findings seen in both the clinical setting as well as rodent models and lends to the predictive validity of this model (Dimitriadis et al., 2017). However, our data yield gives insight into the role of incretins after bariatric surgery in a translational animal model. PYY is primarily responsible for satiety, and the PYY increase after VSG should result in animals' post-VSG consuming less calories resulting in weight loss. Instead, the VSG cohort ate the same amount of calories for the first six months after surgery while calories were matched, and then actually consumed more calories than the sham surgery cohort when exposed to caloric excess, which suggests that incretin changes are not a driving factor for the efficacy of VSG and are instead a downstream effect. Chambers et al. have demonstrated a similar phenomenon in rat models of VSG and have demonstrated that incretins are increased owing to increased gastric emptying after VSG, likely from increased intragastric pressure from the removal of the stomach fundus (Chambers et al., 2012, 2014). Consistent with these rodent studies, in our NHP model, GLP-1 trended toward an increase after VSG. Although gastric emptying was not assessed in our study, changes in gastric transit times and intestinal nutrient delivery and the resultant incretin changes have profound effects on metabolism and can be assessed in future studies to investigate the complex, interrelated mechanisms by which VSG improves metabolic control.

Systems such as the microbiome, metabolome, and immune system have been implicated in the pathogenesis of obesity, and their integration and cross-talk are critical to investigate when modeling how obesity treatments such as bariatric surgery effect change (Lumeng and Saltiel, 2011). We observed changes in the microbiome and metabolome after VSG that have been reported in the clinical literature, with a decrease in the *Firmicutes:Bacteroidetes* ratio in the early postoperative period (1 month) (Campisciano et al., 2018; Debédat et al., 2019; Mulla et al., 2018). These changes occurred while weight loss was the same between the VSG and sham animals in the early postoperative period, suggesting that metabolome and microbiome changes are weight-independent mechanisms by which VSG can confer long-term metabolic improvements. Notably, the *Firmicutes:Bacteroidetes* ratio could be a measure of microbiome health and has been hypothesized to be associated with a lean phenotype (Magne et al., 2020). However, at D180, early postoperative changes were not persistent, highlighting the need to understand microbiome diversity and function as they relate to changes in metabolites and downstream functional effects as an important target for future studies.

We investigated changes in the metabolome after VSG and found that secondary BAs and SCFAs were increased early after VSG. Interestingly, these changes did not persist one year from surgery, while it has been a more persistent effect in humans (Albaugh et al., 2017), perhaps owing to the confounders of metabolite changes such as diet and environment. However, our data demonstrating early increases in BAs and SCFAs suggest a "priming" effect in which VSG results in early microbiome and resultant metabolite changes that then interact with the local immune microenvironment to establish a long-term reduction in VAT inflammation. Primary BAs are excreted by the liver and processed into secondary BAs by the gut microbiota, and thus may be a link between the microbiome and hepatic regulation of glucose metabolism. Similarly, SCFAs are a byproduct of fiber fermentation by the gut microbiota. Recent studies have demonstrated the significant role that secondary BAs and SCFAs play in metabolism, adiposity, and immune system modulation. Albaugh et al. demonstrated that bile diversion improved glucose homeostasis in rodents via an intestinal farnesoid X receptor (FXR)-GLP-1 axis with the mediation of these metabolic changes by the microbiome, highlighting the link between the microbiome, BAs, incretins, and glucose homeostasis (Albaugh et al., 2019). Schmid et al. demonstrated BA signaling pathways such as FXR within adipocytes, suggesting that BAs may decrease AT inflammation and promote lipolysis (Schmid et al., 2019). Tregs have been extensively described in rodent models of obesity as critical in controlling VAT inflammation and contributing to the maintenance of a lean state (Mathis, 2013). Feuerer et al. described VAT Tregs with a specific transcriptome and clonally-expanded TCR repertoire that was reduced in insulin-resistant mice and this was shown by Cipolletta et al. to be driven by the expression of PPARγ by VAT Tregs (Cipolletta et al., 2012; Feuerer et al., 2009). Derivatives of the secondary BA lithocholic acid enhance differentiation of Tregs and reduce Th17 cell differentiation by binding RORγt (Hang et al., 2019). SCFAs such as butyric acid exert beneficial effects through many interrelated mechanisms like enhancing intestinal barrier function and mucosal immunity and altering incretin secretion, and though it is thought to reduce AT inflammation this is less described (Liu et al., 2018; McNabney and Henagan, 2017; Vallianou et al., 2019). Yet BA or SCFA administration alone, while promising in small animals, has lacked full translational efficacy to the clinical setting (Daud et al., 2014; Fluitman et al., 2018; Liu et al., 2018; Reijnders et al., 2016).

Differences in complex, diverse, and interrelated systems such as the metabolome and immune system between lower-order species and primates highlight the importance of using a valid preclinical model with respect to construct and predictive validity. For example, humans and NHPs have similar BA profiles, while mice have a predominance of the BA muricholic acid which has no analog in primates (Straniero et al., 2020). Though the immune system of NHPs has some minor species-specific variation as expected, the NHP and human immune systems are quite similar (Messaoudi et al., 2011). Conversely, the immune system differences between rodents and humans are well-documented, with notable variations in immune education, leukocyte subsets, B and T cell signaling pathways, and cytokines and receptors (Mestas and Hughes, 2004). Selecting an animal model fit for the outcome measure of interest is fundamental to translating findings from our animal models into patient therapies and ensuring appropriate use of animal subjects as outlined by the 3Rs (Eggel and Würbel, 2020; Kirk, 2018). Our reported NHP model provides a translational method for probing the cross-talk between the microbiome, metabolome, and immune system.

Owing to our findings of weight-independent microbiome and metabolome changes in the first month after VSG, we investigated early differences in the immune system with an exploratory cohort to test our hypothesis of a "priming" effect of VSG on the immune system. Interestingly, the immunocytes observed in the PBLs were also seen in the VAT and SAT compartments, indicating a similar level of myeloid and Treg heterogeneity across all three tissue compartments. Upon comparing the phenotype and activation of myeloid cells and Tregs between tissue compartments, we observed that VSG induced expansion of immune regulatory subsets of myeloid cells and Tregs most noticeably in VAT compared to preoperative immunocyte populations.

In the myeloid lineage, we observed 12 distinct cellular populations, and the quantity and phenotype of most of these populations were modulated by VSG. Notably, VSG induced a significant reduction in activated macrophages (population 1) in both AT compartments. Although the prevalence of VAT M1-like macrophages in obesity and polarization toward M2-like macrophages in lean humans and rodents has been well described, the M2 vs. M1 paradigm is increasingly appreciated as less binary and more of a spectrum of macrophage function with multiple phenotypes (Lumeng et al., 2007; Morris et al., 2011; Russo and Lumeng, 2018; Shapouri-Moghaddam et al., 2018). Utilization of CyTOF provides important insights into the polarization of suppressive myeloid cells (defined with classic cell markers as MDSC, M2 macrophages, and DC-10 cells) toward an even more suppressive phenotype with increased expression of CD11b after VSG. A recent study demonstrated that macrophages are reduced in the VAT of patients who have undergone RYGB; however, this observation was made 3 months after bariatric surgery and provides only a late snapshot of macrophages phenotypes in VAT (Kristensen et al., 2017), further supporting the clinical translatability of our model. $CD2^{+}$ monocytes serve as a precursor to DCs and $CD2^{hi}$ monocytes are potent inducers of T cell proliferation and activation (Crawford et al., 1999). We observed a highly expanded population of $CD2^{hi}$ DC-10s (population 10) after VSG in VAT, supporting VSG-mediated induction of a strong anti-inflammatory and suppressive environment in VAT. AT macrophages play a key role in inducing differentiation and proliferation of Tregs in vivo, and PPARγ activation skews monocytes toward an anti-inflammatory M2-like phenotype (Bouhlel et al., 2007; Onodera et al., 2015). In our clustering analysis, the highest expression of PPARγ was observed in the M2-like macrophages (population 9) with strong signatures of activation ($Tbet^{+}$), proliferation ($Ki67^{+}$), and expression of CD49b and CD103 integrins. This observation potentially suggests that PPARγ activation primes monocytes into an enhanced M2-like phenotype, and these PPARγ-primed M2-like macrophages exert more pronounced anti-inflammatory properties. These preliminary observations demonstrate the need for further in-depth dissection of AT macrophage biology, their role in antigen presentation in tissue microenvironments, and the epigenetic, transcriptional, and functional alterations induced by VSG that promote tissue Treg generation.

Obesogenic memory in AT contributes to the ease of relapse/weight regain after weight loss, as weight loss alone likely does not significantly alter VAT inflammation (Sun et al., 2020; Zamarron et al., 2017). We demonstrate a decrease in proliferating $CD4^{+}$ cells in the VAT one month after VSG, indicating its impact on obesogenic memory. Frikke-Schmidt et al. similarly showed in mice that shift in VAT immunocytes after VSG is independent of weight loss, though the specific cell populations were different from this study highlighting the need for our translational model (Frikke-Schmidt et al., 2017). We were able to identify six phenotypically distinct populations of Tregs induced by VSG, including changes in quantity and polarization toward a more regulatory phenotype. We saw a notable increase in PPARγ expression in highly activated tissue Tregs after VSG. Additionally, there was an expansion of these $PPAR\gamma^{hi}$ $FoxP3^{hi}$ Tregs in VAT (populations 3 and 4) demonstrating a highly activated ($CD69^{+}$, $Tbet^{+}$, $LAG\text{-}3^{+}$, $HLA\text{-}DR^{+}$)

tissue-resident effector memory ($CD103^+$, $CD107a^+$) phenotype (Huehn et al., 2004; Rötzschke et al., 2009). These expanded $PPAR\gamma^{hi}$ $FoxP3^{hi}$ Tregs demonstrate a recently activated phenotype ($CD11b^+$) (Christensen et al., 2001) with high migratory potential ($CD11c^+$) (Qualai et al., 2016), suggesting these Tregs are potent in their ability to regulate tissue-specific inflammation. Given the link between PPARγ, metabolite signaling, and Treg polarization, future studies that investigate the longitudinal impact of the SCFA and BA receptor signaling pathways on the behavior and function of T cells in mediating inflammation in response to weight-loss intervention will provide important insights into improving obesity treatments.

A recent study by Fan et al. demonstrates that the expression of CD49b defines the functionally potent subset of mature effector Tregs that recirculate through and survey peripheral tissues (Fan et al., 2018). In our FlowSOM clustering analysis, we found higher expression of CD49b on tissue-resident and resting Tregs (populations 3 and 5, respectively), and the highest CD49b expression on activated migratory Tregs (population 4) across all three tissue compartments. Our results suggest that after VSG, $CD49b^+$ Tregs are substantially expanded in AT and peripheral circulation, conferring a reduction in tissue inflammation. Collectively, these observations surrounding immunocyte phenotypes demonstrate that VSG induces heterogeneous subsets of myeloid cells and Tregs in AT early after VSG.

Remarkably, the immune changes in VAT after VSG were seen up to one year postoperatively in our study suggesting that VSG modulates the obesogenic memory of VAT. Though there was a reduction in anti-inflammatory macrophages after VSG compared to sham surgery, VAT-specific reductions in CLSs suggest that the balance between pro- and anti-inflammatory immunocytes had been shifted by VSG, and a sustained presence of a robust anti-inflammatory phenotype was not required to maintain metabolic benefit. This is consistent with the equalization of BAs and SCFAs seen one year after VSG – as the interactions between metabolites and immunocytes have already occurred early after surgery, persistent elevation of metabolites was no longer needed. Our observation of CLSs in NHPs is consistent with observations in the literature demonstrating an increase in CLSs in the VAT of MUO (Cinti et al., 2005; Murano et al., 2008). Obesity primarily alters the immune landscape in the VAT compared with SAT or peripheral circulation (Cipolletta et al., 2012). Furthermore, our results suggest that the shift of the macrophages to the anti-inflammatory M2 macrophages in the VAT might down-modulate chemotactic signals in the VAT for the recruitment of CD3+ T cells. Our finding of CLS reduction only in the VAT, not in SAT or peripheral circulation, seen after VSG in NHPs gives new insight into the regulation of VAT inflammation by bariatric surgery, bridging mechanistic studies in rodents with observations in clinical trials. Future studies will explore the longitudinal relationships of the interactions between the immune system and metabolites to improve obesity treatments.

We sought predictive validity as the major emphasis in model development, and our NHP model demonstrated excellent forward and reverse translation as previously described with weight loss, weight regain with caloric excess, metabolic improvements, and changes in incretins and BAs in NHPs after VSG as seen in humans. Additionally, performing VSG in outbred, heterogeneous NHP species extends the generalizability of this model. Our preclinical model controlled for confounding variables difficult to account for in human studies, such as diet and caloric intake, activity levels, medications, and environment. The primate model is similarly advantageous with respect to construct validity of the surgical approach as well as comparative anatomy. The surgical approach undertaken in NHPs is homologous to the clinical situation, while VSG in the rodent is dramatically different and most often involves open gastrectomy with a clip and oversew (Figure S12). Rodent models of obesity and bariatric surgery are also limited by significant differences in the gastric and AT anatomy of rodents, notably ruminant gastric pouches and epididymal fat pads (Kararli, 1995; Rao et al., 2010), as well as varied and often high postoperative mortality (Stevenson et al., 2019). The utilization of this primate model in which we are able to control for confounding variables and perform sampling that cannot be conducted in humans in a complex and biologically relevant animal provides a critical bridge between in vitro and rodent modeling of highly promising obesity treatments and the human patient.

Conclusions

In conclusion, we have established successful VSG in NHPs to model the most common obesity treatment approach in humans and demonstrate that VSG induces weight loss and sustained metabolic improvement consistent with the clinical scenario. VSG in NHPs confers metabolic improvement and a shift toward reduced inflammation in the VAT, providing insight into the complex mechanisms by which VSG improves obesity and related diseases. Early, weight-independent mechanistic changes after VSG include an increase in secondary BAs, SCFAs, and a polarization of VAT immunocytes toward a more activated and

regulatory phenotype specifically in the myeloid- and Treg lineage populations. Taken together, these results suggest VSG modulates metabolic control through not only weight loss, but more importantly by impacting the cross-talk between BAs, SCFAs, and the immune system. Evaluation of interrelated, complex functional systems such as metabolomics, transcriptomics, genomics, and immune characterization allows for this model to be used to enhance patient's responsiveness to obesity treatments such as bariatric surgery and catalyze progress from the bench to bedside for innovative therapies for obesity.

Limitations of the study

Reverse translation of successful clinical treatments is a powerful tool to support the selection and validation of animal models; however, our study is not without limitations. These studies were undertaken using modest animal numbers; this was an intentional aspect of our study design. The utilization of a small cohort is consistent with good animal stewardship and the 3Rs to demonstrate feasibility and safety, validate the model, and investigate preliminary findings to establish reference data for powering studies by outcomes of interest. In this case, significant differences in weight loss and metabolic improvement were observed even with small groups sizes, while other factors (i.e., microbiome) were clearly trending but would require larger animal numbers to power future studies if the primary outcome of interest. The lack of a sham surgery control group in our preliminary, short-term study must also be considered when interpreting the immunocyte profiling with CyTOF. We studied these animals in the first month after VSG given equal weight loss and metabolic control between the sham surgery and VSG cohorts during the long-term study. Although comparing post-VSG to pre-VSG in this longitudinal way is a limitation as it does not account for changes that happen after any surgery, it also allows for each animal to act as their own control. We believe this is a reasonable preliminary design in the context of the extensive characterization of sham animals during the long-term study, though of course, future studies will include a sham surgery control. Finally, we used an all-male animal cohort, typical in exploratory studies, which unfortunately contributes to a paucity of literature surrounding obesity in females, despite >70% of bariatric surgery being performed for females (Kizy et al., 2017; Welbourn et al., 2019). The contributions of sex to obesity and metabolic disease are poorly characterized in part owing to the inability to sex-balance clinical studies, though sex differences in immunocytes specifically in relation to obesogenic cues have been observed (Singer et al., 2015). In future studies, our model can be leveraged with a sex-balanced cohort to further evaluate sex-specific contributions to obesity and metabolic disease that cannot be evaluated in humans.

STAR★METHODS

Detailed methods are provided in the online version of this paper and include the following:

- KEY RESOURCES TABLE
- RESOURCE AVAILABILITY
  - Lead contact
  - Materials availability
  - Data and code availability
- EXPERIMENTAL MODEL AND SUBJECT DETAILS
  - Animals
  - Animal handling, training, and preoperative care
- METHOD DETAILS
  - Study design
  - Surgical technique
  - Animal morphometric evaluation
  - Glucose tolerance testing
  - Laboratory testing
- QUANTIFICATION AND STATISTICAL ANALYSIS

SUPPLEMENTAL INFORMATION

Supplemental information can be found online at https://doi.org/10.1016/j.isci.2021.103421.

ACKNOWLEDGMENTS

We gratefully acknowledge the excellent and expert care, husbandry, and training of our animals by the team at the University of Minnesota's Preclinical Research Center. We thank Dr. Michael Goldberg of the University of Minnesota for planning and performance of conventional flow cytometry. We thank the

University of Minnesota Comparative Pathology Shared Resource for processing and preparation of histological sections. This work was funded by endowments from the Jay Phillips Chair and the Robert and Katherine Goodale Chair in Minimally Invasive Surgery, as well as using resources from the University of Minnesota Clinical Immersion Program.

AUTHOR CONTRIBUTIONS

Conceptualization: MLG, SI, SK, JLN, SR, AS (flow cytometry and CyTOF), KMW.

Validation: MLG, JLN, SR, AS (developed/validated 36 metal-tagged antibodies for use in macaques)

Methodology: MLG, SHO, SI, JLJ, SK, JLN, SR, AS, and BH (protocol development/optimization for tissue digestion and SVF harvest from AT), KMW.

Analysis and investigation: MLG, BH, SI, JLJ, JLN, SK, SHO, SR, AS (CyTOF and conventional flow dataset generation/analysis), CS, KMW.

Visualization: JLN, SHO, AS (CyTOF), LHS, KMW.

Funding acquisition: MLG, SI.

Project administration: MLG, JLJ.

Supervision: MLG, SI, SR.

Writing – original draft: JLN, ACS, AS (CyTOF), KMW.

Writing – review & editing: MLG, BH, SI, JLN, SHO, SR, AS, LHS.

DECLARATION OF INTERESTS

The authors declare no competing interests.

INCLUSION AND DIVERSITY

One or more of the authors of this paper self-identifies as an underrepresented ethnic minority in science.
One or more of the authors of this paper self-identifies as a member of the LGBTQ+ community.

Received: July 14, 2021
Revised: October 22, 2021
Accepted: November 4, 2021
Published: December 17, 2021

REFERENCES

(2018). In Diabetes in america, C.C. Cowie, S.S. Casagrande, A. Menke, M.A. Cissell, M.S. Eberhardt, J.B. Meigs, E.W. Gregg, W.C. Knowler, E. Barrett-Connor, D.J. Becker, et al., eds. (National Institute of Diabetes and Digestive and Kidney Diseases (US)).

Affinati, A.H., Esfandiari, N.H., Oral, E.A., and Kraftson, A.T. (2019). Bariatric surgery in the treatment of type 2 diabetes. Curr. Diabetes Rep. *19*, 156. https://doi.org/10.1007/s11892-019-1269-4.

Ahima, R.S., and Lazar, M.A. (2013). Physiology. The health risk of obesity–better metrics imperative. Science *341*, 856–858. https://doi.org/10.1126/science.1241244.

Albaugh, V.L., Banan, B., Ajouz, H., Abumrad, N.N., and Flynn, C.R. (2017). Bile acids and bariatric surgery. Mol. Aspect. Med. *56*, 75–89. https://doi.org/10.1016/j.mam.2017.04.001.

Albaugh, V.L., Banan, B., Antoun, J., Xiong, Y., Guo, Y., Ping, J., Alikhan, M., Clements, B.A., Abumrad, N.N., and Flynn, C.R. (2019). Role of bile acids and glp-1 in mediating the metabolic improvements of bariatric surgery. Gastroenterology *156*, 1041–1051.e1044. https://doi.org/10.1053/j.gastro.2018.11.017.

Arterburn, D., and Gupta, A. (2018). Comparing the outcomes of sleeve gastrectomy and roux-en-y gastric bypass for severe obesity. Jama *319*, 235–237. https://doi.org/10.1001/jama.2017.20449.

Arterburn, D., Wellman, R., Emiliano, A., Smith, S.R., Odegaard, A.O., Murali, S., Williams, N., Coleman, K.J., Courcoulas, A., Coley, R.Y., et al. (2018). Comparative effectiveness and safety of bariatric procedures for weight loss: a pcornet cohort study. Ann. Intern. Med. *169*, 741–750. https://doi.org/10.7326/m17-2786.

Association, A.D. (2018a). 2. Classification and diagnosis of diabetes: standards of medical care in diabetes-2018. Diabetes Care *41*. S13–s27. https://doi.org/10.2337/dc18-S002.

Association, A.D. (2018b). 4. Lifestyle management: standards of medical care in diabetes-2018. Diabetes Care *41*. S38–s50. https://doi.org/10.2337/dc18-S004.

Basukala, P., Jha, B., Yadav, B.K., and Shrestha, P.K. (2018). Determination of insulin resistance and beta-cell function using homeostatic model assessment in type 2 diabetic patients at diagnosis. J. Diabetes Metabol. *9*, 1–11. https://doi.org/10.4172/2155-6156.1000790.

Batterham, R.L., and Cummings, D.E. (2016). Mechanisms of diabetes improvement following bariatric/metabolic surgery. Diabetes Care *39*, 893–901. https://doi.org/10.2337/dc16-0145.

Becker, M., Levings, M.K., and Daniel, C. (2017). Adipose-tissue regulatory t cells: critical players in adipose-immune crosstalk. Eur. J. Immunol. *47*, 1867–1874. https://doi.org/10.1002/eji.201646739.

Belzung, C., and Lemoine, M. (2011). Criteria of validity for animal models of psychiatric disorders: focus on anxiety disorders and depression. Biol. Mood Anxiety Disord. *1*, 9. https://doi.org/10.1186/2045-5380-1-9.

Bersoux, S., Byun, T.H., Chaliki, S.S., and Poole, K.G. (2017). Pharmacotherapy for obesity: what you need to know. Cleve. Clin. J. Med. *84*, 951–958. https://doi.org/10.3949/ccjm.84a.16094.

Blüher, M., and Mantzoros, C.S. (2015). From leptin to other adipokines in health and disease: facts and expectations at the beginning of the 21st century. Metabolism *64*, 131–145. https://doi.org/10.1016/j.metabol.2014.10.016.

Bouhlel, M.A., Derudas, B., Rigamonti, E., Dièvart, R., Brozek, J., Haulon, S., Zawadzki, C., Jude, B., Torpier, G., Marx, N., et al. (2007). Ppargamma activation primes human monocytes into alternative m2 macrophages with anti-inflammatory properties. Cell Metabol. *6*, 137–143. https://doi.org/10.1016/j.cmet.2007.06.010.

Buchwald, H. (2014). The evolution of metabolic/bariatric surgery. Obes. Surg. *24*, 1126–1135. https://doi.org/10.1007/s11695-014-1354-3.

Campisciano, G., Palmisano, S., Cason, C., Giuricin, M., Silvestri, M., Guerra, M., Macor, D., De Manzini, N., Crocé, L.S., and Comar, M. (2018). Gut microbiota characterisation in obese patients before and after bariatric surgery. Benef. Microbes *9*, 367–373. https://doi.org/10.3920/bm2017.0152.

Carlsson, L.M.S., Sjöholm, K., Jacobson, P., Andersson-Assarsson, J.C., Svensson, P.A., Taube, M., Carlsson, B., and Peltonen, M. (2020). Life expectancy after bariatric surgery in the Swedish obese subjects study. N. Engl. J. Med. *383*, 1535–1543. https://doi.org/10.1056/NEJMoa2002449.

Chambers, A.P., Wilson-Perez, H.E., McGrath, S., Grayson, B.E., Ryan, K.K., D'Alessio, D.A., Woods, S.C., Sandoval, D.A., and Seeley, R.J. (2012). Effect of vertical sleeve gastrectomy on food selection and satiation in rats. Am. J. Physiol. Endocrinol. Metab. *303*, E1076–E1084. https://doi.org/10.1152/ajpendo.00211.2012.

Chambers, A.P., Smith, E.P., Begg, D.P., Grayson, B.E., Sisley, S., Greer, T., Sorrell, J., Lemmen, L., LaSance, K., Woods, S.C., et al. (2014). Regulation of gastric emptying rate and its role in nutrient-induced glp-1 secretion in rats after vertical sleeve gastrectomy. Am. J. Physiol. Endocrinol. Metab. *306*, E424–E432. https://doi.org/10.1152/ajpendo.00469.2013.

Chou, K., and Perry, C.M. (2013). Metreleptin: first global approval. Drugs *73*, 989–997. https://doi.org/10.1007/s40265-013-0074-7.

Christensen, J.E., Andreasen, S.O., Christensen, J.P., and Thomsen, A.R. (2001). Cd11b expression as a marker to distinguish between recently activated effector cd8(+) t cells and memory cells. Int. Immunol. *13*, 593–600. https://doi.org/10.1093/intimm/13.4.593.

Cinti, S., Zingaretti, M.C., Cancello, R., Ceresi, E., and Ferrara, P. (2001). Morphologic techniques for the study of brown adipose tissue and white adipose tissue. Methods Mol. Biol. *155*, 21–51. https://doi.org/10.1385/1-59259-231-7:021.

Cinti, S., Mitchell, G., Barbatelli, G., Murano, I., Ceresi, E., Faloia, E., Wang, S., Fortier, M., Greenberg, A.S., and Obin, M.S. (2005). Adipocyte death defines macrophage localization and function in adipose tissue of obese mice and humans. J. Lipid Res. *46*, 2347–2355. https://doi.org/10.1194/jlr.M500294-JLR200.

Cipolletta, D., Feuerer, M., Li, A., Kamei, N., Lee, J., Shoelson, S.E., Benoist, C., and Mathis, D. (2012). Ppar-γ is a major driver of the accumulation and phenotype of adipose tissue treg cells. Nature *486*, 549–553. https://doi.org/10.1038/nature11132.

Classification and diagnosis of diabetes. Sec. 2 (2015). American Diabetes Association.

Clingerman, K.J., and Summers, L. (2005). Development of a body condition scoring system for nonhuman primates using macaca mulatta as a model. Lab. Anim. (Ny) *34*, 31–36. https://doi.org/10.1038/laban0505-31.

Crawford, K., Gabuzda, D., Pantazopoulos, V., Xu, J., Clement, C., Reinherz, E., and Alper, C.A. (1999). Circulating cd2+ monocytes are dendritic cells. J. Immunol. *163*, 5920–5928.

Daud, N.M., Ismail, N.A., Thomas, E.L., Fitzpatrick, J.A., Bell, J.D., Swann, J.R., Costabile, A., Childs, C.E., Pedersen, C., Goldstone, A.P., et al. (2014). The impact of oligofructose on stimulation of gut hormones, appetite regulation and adiposity. Obesity (Silver Spring) *22*, 1430–1438. https://doi.org/10.1002/oby.20754.

Debédat, J., Amouyal, C., Aron-Wisnewsky, J., and Clément, K. (2019). Impact of bariatric surgery on type 2 diabetes: contribution of inflammation and gut microbiome? Semin. Immunopathol. *41*, 461–475. https://doi.org/10.1007/s00281-019-00738-3.

Dimitriadis, G.K., Randeva, M.S., and Miras, A.D. (2017). Potential hormone mechanisms of bariatric surgery. Curr. Obes. Rep. *6*, 253–265. https://doi.org/10.1007/s13679-017-0276-5.

Eggel, M., and Würbel, H. (2020). Internal consistency and compatibility of the 3rs and 3vs principles for project evaluation of animal research. Lab. Anim. *55*, 233–243. https://doi.org/10.1177/0023677220968583.

Fan, X., Moltedo, B., Mendoza, A., Davydov, A.N., Faire, M.B., Mazutis, L., Sharma, R., Pe'er, D., Chudakov, D.M., and Rudensky, A.Y. (2018). Cd49b defines functionally mature treg cells that survey skin and vascular tissues. J. Exp. Med. *215*, 2796–2814. https://doi.org/10.1084/jem.20181442.

Feuerer, M., Herrero, L., Cipolletta, D., Naaz, A., Wong, J., Nayer, A., Lee, J., Goldfine, A.B., Benoist, C., Shoelson, S., et al. (2009). Lean, but not obese, fat is enriched for a unique population of regulatory t cells that affect metabolic parameters. Nat. Med. *15*, 930–939. https://doi.org/10.1038/nm.2002.

Fluitman, K.S., Wijdeveld, M., Nieuwdorp, M., and RG, I.J. (2018). Potential of butyrate to influence food intake in mice and men. Gut *67*, 1203–1204. https://doi.org/10.1136/gutjnl-2017-315543.

Fox, C.S., Massaro, J.M., Hoffmann, U., Pou, K.M., Maurovich-Horvat, P., Liu, C.Y., Vasan, R.S., Murabito, J.M., Meigs, J.B., Cupples, L.A., et al. (2007). Abdominal visceral and subcutaneous adipose tissue compartments: association with metabolic risk factors in the framingham heart study. Circulation *116*, 39–48. https://doi.org/10.1161/circulationaha.106.675355.

Frikke-Schmidt, H., Zamarron, B.F., O'Rourke, R.W., Sandoval, D.A., Lumeng, C.N., and Seeley, R.J. (2017). Weight loss independent changes in adipose tissue macrophage and t cell populations after sleeve gastrectomy in mice. Mol. Metabol. *6*, 317–326. https://doi.org/10.1016/j.molmet.2017.02.004.

Goldrick, R.B. (1967). Morphological changes in the adipocyte during fat deposition and mobilization. Am. J. Physiol. *212*, 777–782. https://doi.org/10.1152/ajplegacy.1967.212.4.777.

Graham, M.L. (2017). Chapter 12: positive reinforcement training and research. In Handbook of Primate Behavioral Management, S.J. Shapiro, ed. (CRC Press), pp. 187–200.

Graham, M.L., and Schuurman, H.J. (2015). Validity of animal models of type 1 diabetes, and strategies to enhance their utility in translational research. Eur. J. Pharmacol. *759*, 221–230. https://doi.org/10.1016/j.ejphar.2015.02.054.

Graham, M.L., Rieke, E.F., Dunning, M., Mutch, L.A., Craig, A.M., Zolondek, E.K., Hering, B.J., Schuurman, H.J., and Bianco, R.W. (2009). A novel alternative placement site and technique for totally implantable vascular access ports in non-human primates. J. Med. Primatol. *38*, 204–212. https://doi.org/10.1111/j.1600-0684.2009.00340.x.

Graham, M.L., Rieke, E.F., Mutch, L.A., Zolondek, E.K., Faig, A.W., Dufour, T.A., Munson, J.W., Kittredge, J.A., and Schuurman, H.J. (2012). Successful implementation of cooperative handling eliminates the need for restraint in a complex non-human primate disease model. J. Med. Primatol. *41*, 89–106. https://doi.org/10.1111/j.1600-0684.2011.00525.x.

Guide for the care and use of laboratory animals (2011), 8 Edition (The National Academies Press).

Halaas, J.L., Boozer, C., Blair-West, J., Fidahusein, N., Denton, D.A., and Friedman, J.M. (1997). Physiological response to long-term peripheral and central leptin infusion in lean and obese

mice. Proc. Natl. Acad. Sci. U S A. *94*, 8878–8883. https://doi.org/10.1073/pnas.94.16.8878.

Hang, S., Paik, D., Yao, L., Kim, E., Trinath, J., Lu, J., Ha, S., Nelson, B.N., Kelly, S.P., Wu, L., et al. (2019). Bile acid metabolites control t(h)17 and t(reg) cell differentiation. Nature *576*, 143–148. https://doi.org/10.1038/s41586-019-1785-z.

Hillmann, B., Al-Ghalith, G.A., Shields-Cutler, R.R., Zhu, Q., Gohl, D.M., Beckman, K.B., Knight, R., and Knights, D. (2018). Evaluating the information content of shallow shotgun metagenomics. mSystems *3*, e00069–18. https://doi.org/10.1128/mSystems.00069-18.

Hocum Stone, L., Oppler, S.H., Nugent, J.L., Gresch, S., Hering, B.J., Murtaugh, M.P., Hegstad-Davies, R.L., Ramachandran, S., and Graham, M.L. (2021). Serum cytokine profiles in healthy nonhuman primates are blunted by sedation and demonstrate sexual dimorphism as detected by a validated multiplex immunoassay. Sci. Rep. *11*, 2340. https://doi.org/10.1038/s41598-021-81953-7.

Huehn, J., Siegmund, K., Lehmann, J.C., Siewert, C., Haubold, U., Feuerer, M., Debes, G.F., Lauber, J., Frey, O., Przybylski, G.K., et al. (2004). Developmental stage, phenotype, and migration distinguish naive- and effector/memory-like cd4+ regulatory t cells. J. Exp. Med. *199*, 303–313. https://doi.org/10.1084/jem.20031562.

Ikramuddin, S. (2015). Bariatric surgery and bone health. Obesity (Silver Spring) *23*, 2323. https://doi.org/10.1002/oby.21260.

Ikramuddin, S., and Livingston, E.H. (2013). New insights on bariatric surgery outcomes. JAMA *310*, 2401–2402. https://doi.org/10.1001/jama.2013.280927.

Ikramuddin, S., Korner, J., Lee, W.J., Connett, J.E., Inabnet, W.B., Billington, C.J., Thomas, A.J., Leslie, D.B., Chong, K., Jeffery, R.W., et al. (2013). Roux-en-y gastric bypass vs intensive medical management for the control of type 2 diabetes, hypertension, and hyperlipidemia: the diabetes surgery study randomized clinical trial. Jama *309*, 2240–2249. https://doi.org/10.1001/jama.2013.5835.

Jen, K.L., Hansen, B.C., and Metzger, B.L. (1985). Adiposity, anthropometric measures, and plasma insulin levels of rhesus monkeys. Int. J. Obes. *9*, 213–224.

Johnson, L.M., Ikramuddin, S., Leslie, D.B., Slusarek, B., and Killeen, A.A. (2019). Analysis of vitamin levels and deficiencies in bariatric surgery patients: a single-institutional analysis. Surg. Obes. Relat. Dis. *15*, 1146–1152. https://doi.org/10.1016/j.soard.2019.04.028.

Kararli, T.T. (1995). Comparison of the gastrointestinal anatomy, physiology, and biochemistry of humans and commonly used laboratory animals. Biopharm. Drug Dispos. *16*, 351–380. https://doi.org/10.1002/bdd.2510160502.

Khera, R., Murad, M.H., Chandar, A.K., Dulai, P.S., Wang, Z., Prokop, L.J., Loomba, R., Camilleri, M., and Singh, S. (2016). Association of pharmacological treatments for obesity with weight loss and adverse events: a systematic review and meta-analysis. Jama *315*, 2424–2434. https://doi.org/10.1001/jama.2016.7602.

Kirk, R.G.W. (2018). Recovering the principles of humane experimental technique: the 3rs and the human essence of animal research. Sci. Technol. Hum. Val. *43*, 622–648. https://doi.org/10.1177/0162243917726579.

Kizy, S., Jahansouz, C., Downey, M.C., Hevelone, N., Ikramuddin, S., and Leslie, D. (2017). National trends in bariatric surgery 2012-2015: demographics, procedure selection, readmissions, and cost. Obes. Surg. *27*, 2933–2939. https://doi.org/10.1007/s11695-017-2719-1.

Kleinert, M., Clemmensen, C., Hofmann, S.M., Moore, M.C., Renner, S., Woods, S.C., Huypens, P., Beckers, J., de Angelis, M.H., Schurmann, A., et al. (2018). Animal models of obesity and diabetes mellitus. Nat. Rev. Endocrinol. *14*, 140–162. https://doi.org/10.1038/nrendo.2017.161.

Kristensen, M.D., Lund, M.T., Hansen, M., Poulsen, S.S., Ploug, T., Dela, F., Helge, J.W., and Prats, C. (2017). Macrophage area content and phenotype in hepatic and adipose tissue in patients with obesity undergoing roux-en-y gastric bypass. Obesity (Silver Spring) *25*, 1921–1931. https://doi.org/10.1002/oby.21964.

Kumanyika, S., and Dietz, W.H. (2020). Solving population-wide obesity - progress and future prospects. N. Engl. J. Med. *383*, 2197–2200. https://doi.org/10.1056/NEJMp2029646.

Ley, R.E., Bäckhed, F., Turnbaugh, P., Lozupone, C.A., Knight, R.D., and Gordon, J.I. (2005). Obesity alters gut microbial ecology. Proc. Natl. Acad. Sci. U S A. *102*, 11070–11075. https://doi.org/10.1073/pnas.0504978102.

Ley, R.E., Turnbaugh, P.J., Klein, S., and Gordon, J.I. (2006). Microbial ecology: human gut microbes associated with obesity. Nature *444*, 1022–1023. https://doi.org/10.1038/4441022a.

Liu, H., Wang, J., He, T., Becker, S., Zhang, G., Li, D., and Ma, X. (2018). Butyrate: a double-edged sword for health? Adv. Nutr. *9*, 21–29. https://doi.org/10.1093/advances/nmx009.

Longo, M., Zatterale, F., Naderi, J., Parrillo, L., Formisano, P., Raciti, G.A., Beguinot, F., and Miele, C. (2019). Adipose tissue dysfunction as determinant of obesity-associated metabolic complications. Int. J. Mol. Sci. *20*, 2358. https://doi.org/10.3390/ijms20092358.

Lumeng, C.N., and Saltiel, A.R. (2011). Inflammatory links between obesity and metabolic disease. J. Clin. Invest. *121*, 2111–2117. https://doi.org/10.1172/jci57132.

Lumeng, C.N., Bodzin, J.L., and Saltiel, A.R. (2007). Obesity induces a phenotypic switch in adipose tissue macrophage polarization. J. Clin. Invest. *117*, 175–184. https://doi.org/10.1172/jci29881.

Magne, F., Gotteland, M., Gauthier, L., Zazueta, A., Pesoa, S., Navarrete, P., and Balamurugan, R. (2020). The firmicutes/bacteroidetes ratio: a relevant marker of gut dysbiosis in obese patients? Nutrients *12*, 1474. https://doi.org/10.3390/nu12051474.

Mathis, D. (2013). Immunological goings-on in visceral adipose tissue. Cell Metabol. *17*, 851–859. https://doi.org/10.1016/j.cmet.2013.05.008.

McNabney, S.M., and Henagan, T.M. (2017). Short chain fatty acids in the colon and peripheral tissues: a focus on butyrate, colon cancer, obesity and insulin resistance. Nutrients *9*, 1348. https://doi.org/10.3390/nu9121348.

Messaoudi, I., Estep, R., Robinson, B., and Wong, S.W. (2011). Nonhuman primate models of human immunology. Antioxid. Redox Signal *14*, 261–273. https://doi.org/10.1089/ars.2010.3241.

Mestas, J., and Hughes, C.C. (2004). Of mice and not men: differences between mouse and human immunology. J. Immunol. *172*, 2731–2738. https://doi.org/10.4049/jimmunol.172.5.2731.

Mingrone, G., Panunzi, S., De Gaetano, A., Guidone, C., Iaconelli, A., Nanni, G., Castagneto, M., Bornstein, S., and Rubino, F. (2015). Bariatric-metabolic surgery versus conventional medical treatment in obese patients with type 2 diabetes: 5 year follow-up of an open-label, single-centre, randomised controlled trial. Lancet *386*, 964–973. https://doi.org/10.1016/s0140-6736(15)00075-6.

Morris, D.L., Singer, K., and Lumeng, C.N. (2011). Adipose tissue macrophages: phenotypic plasticity and diversity in lean and obese states. Curr. Opin. Clin. Nutr. Metab. Care *14*, 341–346. https://doi.org/10.1097/MCO.0b013e328347970b.

Mulla, C.M., Middelbeek, R.J.W., and Patti, M.E. (2018). Mechanisms of weight loss and improved metabolism following bariatric surgery. Ann. N. Y. Acad. Sci. *1411*, 53–64. https://doi.org/10.1111/nyas.13409.

Murano, I., Barbatelli, G., Parisani, V., Latini, C., Muzzonigro, G., Castellucci, M., and Cinti, S. (2008). Dead adipocytes, detected as crown-like structures, are prevalent in visceral fat depots of genetically obese mice. J. Lipid Res. *49*, 1562–1568. https://doi.org/10.1194/jlr.M800019-JLR200.

WHO (2020). Obesity and overweight. https://www.who.int/news-room/fact-sheets/detail/obesity-and-overweight.

O'Neil, P.M., Birkenfeld, A.L., McGowan, B., Mosenzon, O., Pedersen, S.D., Wharton, S., Carson, C.G., Jepsen, C.H., Kabisch, M., and Wilding, J.P.H. (2018). Efficacy and safety of semaglutide compared with liraglutide and placebo for weight loss in patients with obesity: a randomised, double-blind, placebo and active controlled, dose-ranging, phase 2 trial. Lancet *392*, 637–649. https://doi.org/10.1016/s0140-6736(18)31773-2.

Onodera, T., Fukuhara, A., Jang, M.H., Shin, J., Aoi, K., Kikuta, J., Otsuki, M., Ishii, M., and Shimomura, I. (2015). Adipose tissue macrophages induce ppary-high foxp3(+) regulatory t cells. Sci. Rep. *5*, 16801. https://doi.org/10.1038/srep16801.

Ooi, G.J., Burton, P.R., Bayliss, J., Raajendiran, A., Earnest, A., Laurie, C., Kemp, W.W., McLean, C.A., Roberts, S.K., Watt, M.J., et al. (2019). Effect of body mass index, metabolic health and adipose tissue inflammation on the severity of non-alcoholic fatty liver disease in bariatric surgical patients: a prospective study. Obes.

Surg. *29*, 99–108. https://doi.org/10.1007/s11695-018-3479-2.

Panduro, M., Benoist, C., and Mathis, D. (2016). Tissue tregs. Annu. Rev. Immunol. *34*, 609–633. https://doi.org/10.1146/annurev-immunol-032712-095948.

Phillips, C.M. (2017). Metabolically healthy obesity across the life course: epidemiology, determinants, and implications. Ann. N. Y. Acad. Sci. *1391*, 85–100. https://doi.org/10.1111/nyas.13230.

Qualai, J., Li, L.X., Cantero, J., Tarrats, A., Fernández, M.A., Sumoy, L., Rodolosse, A., McSorley, S.J., and Genescà, M. (2016). Expression of cd11c is associated with unconventional activated t cell subsets with high migratory potential. PLoS One *11*, e0154253. https://doi.org/10.1371/journal.pone.0154253.

Rao, R.S., Rao, V., and Kini, S. (2010). Animal models in bariatric surgery–a review of the surgical techniques and postsurgical physiology. Obes. Surg. *20*, 1293–1305. https://doi.org/10.1007/s11695-010-0135-x.

Reges, O., Greenland, P., Dicker, D., Leibowitz, M., Hoshen, M., Gofer, I., Rasmussen-Torvik, L.J., and Balicer, R.D. (2018). Association of bariatric surgery using laparoscopic banding, roux-en-y gastric bypass, or laparoscopic sleeve gastrectomy vs usual care obesity management with all-cause mortality. Jama *319*, 279–290. https://doi.org/10.1001/jama.2017.20513.

Reijnders, D., Goossens, G.H., Hermes, G.D., Neis, E.P., van der Beek, C.M., Most, J., Holst, J.J., Lenaerts, K., Kootte, R.S., Nieuwdorp, M., et al. (2016). Effects of gut microbiota manipulation by antibiotics on host metabolism in obese humans: a randomized double-blind placebo-controlled trial. Cell Metabol. *24*, 63–74. https://doi.org/10.1016/j.cmet.2016.06.016.

Rötzschke, O., Borsellino, G., Battistini, L., Falk, K., and Kleinewietfeld, M. (2009). In vivo-activated cd103+ foxp3+ tregs: of men and mice. Blood *113*, 2119–2120. https://doi.org/10.1182/blood-2008-11-188847.

Russo, L., and Lumeng, C.N. (2018). Properties and functions of adipose tissue macrophages in obesity. Immunology *155*, 407–417. https://doi.org/10.1111/imm.13002.

Schauer, P.R., Bhatt, D.L., Kirwan, J.P., Wolski, K., Brethauer, S.A., Navaneethan, S.D., Aminian, A., Pothier, C.E., Kim, E.S., Nissen, S.E., et al. (2014). Bariatric surgery versus intensive medical therapy for diabetes–3-year outcomes. N. Engl. J. Med. *370*, 2002–2013. https://doi.org/10.1056/NEJMoa1401329.

Schmid, A., Schlegel, J., Thomalla, M., Karrasch, T., and Schäffler, A. (2019). Evidence of functional bile acid signaling pathways in adipocytes. Mol. Cell. Endocrinol. *483*, 1–10. https://doi.org/10.1016/j.mce.2018.12.006.

Schneider, C., Rasband, W., and Eliceiri, K. (2012). NIH Image to ImageJ: 25 years of image analysis. Nature Methods *9*, 671–675. https://doi.org/10.1038/nmeth.2089.

Shah, A., and Laferrère, B. (2017). Diabetes after bariatric surgery. Can. J. Diabetes *41*, 401–406. https://doi.org/10.1016/j.jcjd.2016.12.009.

Shapouri-Moghaddam, A., Mohammadian, S., Vazini, H., Taghadosi, M., Esmaeili, S.A., Mardani, F., Seifi, B., Mohammadi, A., Afshari, J.T., and Sahebkar, A. (2018). Macrophage plasticity, polarization, and function in health and disease. J. Cell. Physiol. *233*, 6425–6440. https://doi.org/10.1002/jcp.26429.

Singer, K., Maley, N., Mergian, T., DelProposto, J., Cho, K.W., Zamarron, B.F., Martinez-Santibanez, G., Geletka, L., Muir, L., Wachowiak, P., et al. (2015). Differences in hematopoietic stem cells contribute to sexually dimorphic inflammatory responses to high fat diet-induced obesity. J. Biol. Chem. *290*, 13250–13262. https://doi.org/10.1074/jbc.M114.634568.

Stevenson, M., Lee, J., Lau, R.G., Brathwaite, C.E.M., and Ragolia, L. (2019). Surgical mouse models of vertical sleeve gastrectomy and roux-en y gastric bypass: a review. Obes. Surg. *29*, 4084–4094. https://doi.org/10.1007/s11695-019-04205-8.

Straniero, S., Laskar, A., Savva, C., Härdfeldt, J., Angelin, B., and Rudling, M. (2020). Of mice and men: murine bile acids explain species differences in the regulation of bile acid and cholesterol metabolism. J. Lipid Res. *61*, 480–491. https://doi.org/10.1194/jlr.RA119000307.

Sun, M., Zheng, S., Gao, X., and Lin, Z. (2020). The role of immune cells in obesogenic memory. Cell. Mol. Immunol. *17*, 884–886. https://doi.org/10.1038/s41423-020-0448-1.

Truong, D.T., Franzosa, E.A., Tickle, T.L., Scholz, M., Weingart, G., Pasolli, E., Tett, A., Huttenhower, C., and Segata, N. (2015). Metaphlan2 for enhanced metagenomic taxonomic profiling. Nat. Methods *12*, 902–903. https://doi.org/10.1038/nmeth.3589.

Turnbaugh, P.J., Hamady, M., Yatsunenko, T., Cantarel, B.L., Duncan, A., Ley, R.E., Sogin, M.L., Jones, W.J., Roe, B.A., Affourtit, J.P., et al. (2009). A core gut microbiome in obese and lean twins. Nature *457*, 480–484. https://doi.org/10.1038/nature07540.

Vallianou, N., Stratigou, T., Christodoulatos, G.S., and Dalamaga, M. (2019). Understanding the role of the gut microbiome and microbial metabolites in obesity and obesity-associated metabolic disorders: current evidence and perspectives. Curr. Obes. Rep. *8*, 317–332. https://doi.org/10.1007/s13679-019-00352-2.

Vaughan, K.L., and Mattison, J.A. (2016). Obesity and aging in humans and nonhuman primates: a mini-review. Gerontology *62*, 611–617. https://doi.org/10.1159/000445800.

Vickers, S.P., Jackson, H.C., and Cheetham, S.C. (2011). The utility of animal models to evaluate novel anti-obesity agents. Br. J. Pharmacol. *164*, 1248–1262. https://doi.org/10.1111/j.1476-5381.2011.01245.x.

Vujkovic-Cvijin, I., Sklar, J., Jiang, L., Natarajan, L., Knight, R., and Belkaid, Y. (2020). Host variables confound gut microbiota studies of human disease. Nature *587*, 448–454. https://doi.org/10.1038/s41586-020-2881-9.

Wagner, J.D., Kavanagh, K., Ward, G.M., Auerbach, B.J., Harwood, H.J., Jr., and Kaplan, J.R. (2006). Old world nonhuman primate models of type 2 diabetes mellitus. ILAR J. *47*, 259–271. https://doi.org/10.1093/ilar.47.3.259.

Wang, L., Zhao, R.P., Song, X.Y., and Wu, W.F. (2019). Targeting erβ in macrophage reduces crown-like structures in adipose tissue by inhibiting osteopontin and hif-1α. Sci. Rep. *9*, 15762. https://doi.org/10.1038/s41598-019-52265-8.

Welbourn, R., Hollyman, M., Kinsman, R., Dixon, J., Liem, R., Ottosson, J., Ramos, A., Våge, V., Al-Sabah, S., Brown, W., et al. (2019). Bariatric surgery worldwide: baseline demographic description and one-year outcomes from the fourth ifso global registry report 2018. Obes. Surg. *29*, 782–795. https://doi.org/10.1007/s11695-018-3593-1.

Willner, P. (1984). The validity of animal models of depression. Psychopharmacology (Berl) *83*, 1–16. https://doi.org/10.1007/bf00427414.

Wing, R.R., Bolin, P., Brancati, F.L., Bray, G.A., Clark, J.M., Coday, M., Crow, R.S., Curtis, J.M., Egan, C.M., Espeland, M.A., et al. (2013). Cardiovascular effects of intensive lifestyle intervention in type 2 diabetes. N. Engl. J. Med. *369*, 145–154. https://doi.org/10.1056/NEJMoa1212914.

De Winter, J.C. (2013). Using the student's t-test with extremely small sample sizes. Pract. Assess. Res. Eval. *18*, 10.

Wu, D., Yue, F., Zou, C., Chan, P., and Alex Zhang, Y. (2012). Analysis of glucose metabolism in cynomolgus monkeys during aging. Biogerontology *13*, 147–155. https://doi.org/10.1007/s10522-011-9364-1.

Yanovski, S.Z., and Yanovski, J.A. (2021). Progress in pharmacotherapy for obesity. Jama *326*, 129–130. https://doi.org/10.1001/jama.2021.9486.

Yu, Y.H. (2017). Making sense of metabolic obesity and hedonic obesity. J. Diabetes *9*, 656–666. https://doi.org/10.1111/1753-0407.12529.

Zamarron, B.F., Mergian, T.A., Cho, K.W., Martinez-Santibanez, G., Luan, D., Singer, K., DelProposto, J.L., Geletka, L.M., Muir, L.A., and Lumeng, C.N. (2017). Macrophage proliferation sustains adipose tissue inflammation in formerly obese mice. Diabetes *66*, 392–406. https://doi.org/10.2337/db16-0500.

Zhao, S., Kusminski, C.M., Elmquist, J.K., and Scherer, P.E. (2020). Leptin: less is more. Diabetes *69*, 823–829. https://doi.org/10.2337/dbi19-0018.

STAR★METHODS

KEY RESOURCES TABLE

REAGENT or RESOURCE	SOURCE	IDENTIFIER
Antibodies		
CD2	BioLegend	Cat#300212; Clone: RPA-210; RRID:AB_10900259
CD3	Fluidigm	Cat#3170007B; Clone: SP34-2
CD3	Bio-Rad	Cat#S2367
CD4	Fluidigm	Cat#3145001B; Clone: 5C3; RRID: AB_2661789
CD8a	Fluidigm	Cat#3146001B; Clone: RPA-T8; RRID: AB_2687641
CD11b	Fluidigm	Cat#3209003B; Clone: Mac-1;RRID: AB_2687654
CD11c	Tonbo	Cat#70-0116-U100; Clone:3.9; RRID:AB_2621485
CD14	Fluidigm	Cat#3175015B; Clone: M5E2; RRID: AB2811083
CD16	Fluidigm	Cat#3165001B; Clone: 3G8; RRID: AB_2802109
CD19	BioLegend	Cat#392502; Clone: 4G7; RRID: AB_2721738
CD20	Fluidigm	Cat#3171012B; Clone: 2H7; RRID: AB_2802112
CD24	Abcam	Cat#ab134375; Clone: SN3
CD25	BD Biosciences	Cat#5545429; Clone: M-A251
CD27	BD Biosciences	Cat#555439; Clone: M-T271
CD28	Tonbo	Cat#70-0289-U100; Clone: CD28.2; RRID: AB_2621493
CD33	Miltenyi	Cat#130-108-039; Clone: AC104.3E3; RRID: AB_2660358
CD38	Fluidigm	Cat#3167001B; Clone: HIT2; RRID: AB_2802110
CD40	Fluidigm	Cat#3142010B; Clone: 5C3
CD45	BD Biosciences	Cat#552566; Clone: D058-1283; RRID: AB_394433
CD49b	BD Biosciences	Cat#555497; Clone: AK-7; RRID: AB_395887
CD68	BioLegend	Cat#333802; Clone: Y1/82A; RRID: AB_1089058
CD69	BioLegend	Cat#310939; Clone: FN50; RRID: AB_2562827
CD95	Fluidigm	Cat#3163008B; Clone: DX2
CD103	Bio-Rad	Cat#MCA708; Clone: 2G5.1; RRID: AB_321984
CD123	BD Biosciences	Cat#554526; Clone: 7G3; RRID: AB_395454
CD127	Invitrogen	Cat#14-1278-82; Clone: ebioRDR5; RRID: AB_657591
CD141	BD Bioscience	Cat#559780; Clone: 1A4; RRID: AB_397321
CD163	BD Biosciences	Cat#556017; Clone: GH/61; RRID: AB_396295
CD206	BD Biosciences	Cat#555953; Clone: 19.2; RRID: AB_396249
FoxP3	BioLegend	Cat#320102; Clone: 206D; RRID: AB_430881
HLA-DR	Fluidigm	Cat#3174001B; Clone: L243; RRID: AB_2665397
IBA-1	Abcam	Cat#ab107159; RRID: AB_10972670
iNKT(TCRVα24-Jα18)	BioLegend	Cat#342902; Clone: 6B11; RRID: AB_2229301
Ki67	BD Biosciences	Cat#556003; Clone: B56; RRID: AB_396287
LAG-3	R&D Systems	Cat#FAB2319P; Clone: polyclonal; RRID: AB_2133351
MAIT	BioLegend	Cat#305602; Clone: Va7.2
PPARγ	Bioss Antibodies	Cat#bs-4590R; Clone: PolySb
Tbet	Fluidigm	Cat#3161014B; Clone: eBio4B10; RRID: AB_2858233
Chemicals, peptides, and recombinant proteins		
Human TruStain FcX Fc Receptor Blocking Solution	BioLegend	Cat#422302
Maxpar® PBS—500 mL	Fluidigm	Cat#201058

(*Continued on next page*)

Continued

REAGENT or RESOURCE	SOURCE	IDENTIFIER
Maxpar® Perm-S Buffer—250 mL	Fluidigm	Cat#201066
Maxpar® Fix and Perm Buffer—100 mL	Fluidigm	Cat#201067
Maxpar® Cell Staining Buffer	Fluidigm	Cat#201068
Maxpar® Water—500 mL	Fluidigm	Cat#201069
Critical commercial assays		
DNeasy 96 PowerSoil Pro Kit	Qiagen	Cat#47017
Human C-Peptide RIA	Millipore-Sigma	Cat#HCP-20K
Maxpar® X8 Antibody Labeling Kit—4 Rxn; Metal Tag: 141Pr	Fluidigm	Cat#201141A
Maxpar® X8 Antibody Labeling Kit—4 Rxn; Metal Tag: 143Nd	Fluidigm	Cat#201143A
Maxpar® X8 Antibody Labeling Kit—4 Rxn; Metal Tag: 144Nd	Fluidigm	Cat#201144A
Maxpar® X8 Antibody Labeling Kit—4 Rxn; Metal Tag: 147Sm	Fluidigm	Cat#201147A
Maxpar® X8 Antibody Labeling Kit—4 Rxn; Metal Tag: 148Nd	Fluidigm	Cat#201148A
Maxpar® X8 Antibody Labeling Kit—4 Rxn; Metal Tag: 149Sm	Fluidigm	Cat#201149A
Maxpar® X8 Antibody Labeling Kit—4 Rxn; Metal Tag: 150Nd	Fluidigm	Cat#201150A
Maxpar® X8 Antibody Labeling Kit—4 Rxn; Metal Tag: 151Eu	Fluidigm	Cat#201151A
Maxpar® X8 Antibody Labeling Kit—4 Rxn; Metal Tag: 152Sm	Fluidigm	Cat#201152A
Maxpar® X8 Antibody Labeling Kit—4 Rxn; Metal Tag: 153Eu	Fluidigm	Cat#201153A
Maxpar® X8 Antibody Labeling Kit—4 Rxn; Metal Tag: 154Sm	Fluidigm	Cat#201154A
Maxpar® X8 Antibody Labeling Kit—4 Rxn; Metal Tag: 155Gd	Fluidigm	Cat#201155A
Maxpar® X8 Antibody Labeling Kit—4 Rxn; Metal Tag: 156Gd	Fluidigm	Cat#201156A
Maxpar® X8 Antibody Labeling Kit—4 Rxn; Metal Tag: 158Gd	Fluidigm	Cat#201158A
Maxpar® X8 Antibody Labeling Kit—4 Rxn; Metal Tag: 159Tb	Fluidigm	Cat#201159A
Maxpar® X8 Antibody Labeling Kit—4 Rxn; Metal Tag: 160Gd	Fluidigm	Cat#201160A
Maxpar® X8 Antibody Labeling Kit—4 Rxn; Metal Tag: 162Dy	Fluidigm	Cat#201162A
Maxpar® X8 Antibody Labeling Kit—4 Rxn; Metal Tag: 163Dy	Fluidigm	Cat#201163A
Maxpar® X8 Antibody Labeling Kit—4 Rxn; Metal Tag:166Er	Fluidigm	Cat#201166A
Maxpar® X8 Antibody Labeling Kit—4 Rxn; Metal Tag: 168Er	Fluidigm	Cat#201168A
Maxpar® X8 Antibody Labeling Kit—4 Rxn; Metal Tag: 169Tm	Fluidigm	Cat#201169A

(*Continued on next page*)

Continued

REAGENT or RESOURCE	SOURCE	IDENTIFIER
Maxpar® X8 Antibody Labeling Kit—4 Rxn; Metal Tag: 172Yb	Fluidigm	Cat#201172A
Maxpar® X8 Antibody Labeling Kit—4 Rxn; Metal Tag: 173Yb	Fluidigm	Cat#201173A
Maxpar® X8 Antibody Labeling Kit—4 Rxn; Metal Tag: 176Lu	Fluidigm	Cat#201176A
Milliplex MAP Non-human Primate Metabolic Magnetic Bead Panel - Metabolism Multiplex Assay	Millipore-Sigma	Cat#NHPMHMAG-45K
Software and algorithms		
Aperio ImageScope	Leica Biosystems	https://www.leicabiosystems.com/digital-pathology/manage/aperio-imagescope/
BioRender	BioRender	https://biorender.com/
FlowJo	BD Biosciences	https://www.flowjo.com/
FlowSOM FlowJo Plugin	BD Biosciences	https://www.flowjo.com/
ImageJ	Schneider et al., 2012	https://imagej.nih.gov/ij/
Prism	GraphPad Software	https://www.graphpad.com/
tSNE FlowJo Plugin	BD Biosciences	https://www.flowjo.com/
Other		
Teklad global 25% protein primate diet	Envigo	Cat#2055C

RESOURCE AVAILABILITY

Lead contact

Further information and requests for resources and reagents should be directed to and will be fulfilled by the lead contact, Dr. Melanie Graham (graha066@umn.edu).

Materials availability

This study did not generate new unique reagents.

Data and code availability

- All data in this paper will be shared by the lead contact upon request.
- This paper does not report original code.
- Any additional information required to reanalyze the data reported in this paper is available from the lead contact upon request.

EXPERIMENTAL MODEL AND SUBJECT DETAILS

Animals

This study was approved by the University of Minnesota Institutional Animal Care and Use Committee and was conducted in compliance with the Animal Welfare Act, adhering to principles stated in the NIH Guide for Care and Use of Laboratory Animals (Guide for the care and use of laboratory animals, 2011). All animals were purchased from an institutionally approved commercial vendor after passing a full physical examination and pathogen screening including *Cercopithecine herpesvirus* 1, measles, tuberculosis, simian immunodeficiency virus, simian T-cell lymphotropic virus, and simian type D retrovirus.

For the long-term (one-year) study, six spontaneously obese male Mauritian origin cynomolgus macaques (*Macaca fascicularis*) were paired by weight, BCS, morphometric parameters, and fasting c-peptide levels (Table S1). All animals demonstrated normal fasting blood glucose and HbA1c (Wagner et al., 2006) (Tables S1, S2, and S3). We selected animals to model the criteria outlined by the ASMBS in the clinical situation

(e.g. BMI ≥ 40, or more than 100 pounds overweight and inability to achieve a healthy weight loss sustained for a period of time with prior weight loss efforts). These animals developed obesity on standard diet, not high fat or high carbohydrate, and remained obese on a high protein diet for approximately 6 months prior to enrollment. After pairing, one subject from each pair was randomized using an electronic tool for VSG (n=3) and the other was assigned to the sham operation (n=3). We selected a small sample size (n=3 for each group) as we were evaluating the VSG model in NHPs for the first time with the intention of gathering evidence regarding this model's future value in more complex experimental designs. Animals were aged 5.7-20.4 years (median 9.4 years) at the time of surgery and weighed 11.3-16.4 kg (median 12.8 kg).

For the short-term (one-month) study, three spontaneously obese male Indian-origin rhesus macaques (*Macaca mulatta*) were identified to undergo VSG. Animals were aged 9.4-10.4 years (median 9.5 years) at the time of surgery and weighed 13.1-15.4 kg (median 14.1 kg). One animal in the short-term study developed sepsis and was euthanized on D6 and excluded from any postoperative analyses as described in Results.

Animal handling, training, and preoperative care

Behavioral management training was employed to eliminate the need for restraint and encourage positive coping behaviors during procedures and testing. To realize the need for frequent blood draws while avoiding confounding effects from restraint, sedation, and pain, all animals were implanted with single-incision peripherally inserted vascular access ports. Antibiotic prophylaxis with 50 mg/kg cefazolin IM was given within 60 minutes of the operative procedure, aseptically prepped, and general anesthesia achieved with inhalation isoflurane and 1% lidocaine delivered locally at the intended incision site. A small vertical 1–1.5 cm incision was made lateral to the saphenous vein distal to the knee and the saphenous vein was visualized using blunt dissection. The catheter was passed proximally into the lumen of the partially transected saphenous vein and advanced centrally into the inferior vena cava. Using the same incision as a starting point, a pocket was bluntly dissected to accommodate the port head. The incision was closed in a normal fashion. Nonsteroidal anti-inflammatory drugs including ketoprofen (1 mg/kg IM) or ibuprofen (10-15 mg/kg PO) and an opioid, buprenorphine (0.01-0.03 mg/kg IM) were used for multimodal analgesic coverage in the 72 hour postoperative period (Graham et al., 2009). No breakthrough pain was observed during postoperative care. All animals were trained to present the port in their homecage as part of a larger cooperative behavioral management program(Graham, 2017; Graham et al., 2012) .

Animals were fed a standardized diet (2055C Certified Teklad Global 25% Protein Primate Diet, Envigo, Madison, WI, USA) with 32% of calories derived from protein, 14% from fats, and 54% from carbohydrates. A standardized enrichment program was used for the duration of the study, including fresh fruits and vegetables, grains, beans, and nuts, as well as a children's multivitamin, 2000 IU vitamin D, and 500 mcg vitamin B12. Baseline free feeding consumption patterns were established prior to the experimental protocol by offering ad libitum access to diet, which resulted in an average intake of 41.9 kcal/kg/day. All animals were offered ad lib access to water.

Animal behavior and clinical status were evaluated at least twice daily. Scheduled physical examinations per protocol and semiannual comprehensive veterinary examinations were performed on all animals. Animals were singly housed due to failed attempts at compatible direct contact pairing but remained in close proximity with social conspecifics maintaining visual, auditory, and olfactory contact at all times. An environmental enrichment program including social play, toys, music, and regularly scheduled access to a large exercise and swimming area was provided to encourage sensory engagement, enhance foraging behavior and novelty seeking, promote mental stimulation, increase exploration, play, and activity levels, and strengthen social behaviors, increasing the proportion of time animals spent on species-typical behaviors. All animals enrolled in this study were offered equal access and time for exercise and identical enrichment activities.

METHOD DETAILS

Study design

For the long-term study, the six study animals were followed for 365 days postoperatively. Preoperative baseline and postoperative interval profiling included weights, body dimensions, BCSs, fasting glucose, fasting c-peptide, HgbA1c, complete blood counts, liver enzymes, triglyceride and cholesterol levels,

IVGTT, OGTT, and incretin levels. Animals underwent weekly blood sampling (± 2 day performance window) and scheduled metabolic testing (±5 day performance window). IVGTTs were performed preoperatively and on D14, D35, D120, and D345. OGTTs were performed preoperatively and on D75, D150 and D360. VAT and SAT were collected during surgery and at necropsy (Figure 2A). SAT samples were collected immediately after incision minimizing manipulation at the camera trocar port. VAT samples were collected from the greater omentum near the curvature of the stomach using a harmonic scalpel. At necropsy the entire residual omentum was collected, and sampled at the distal omentum to avoid sampling areas that might have been altered by previous surgical manipulation, similarly SAT was collected in the lower right abdominal quadrant, avoiding previous trocar placement sites. To ensure sampling consistency, all tissue sampling was done by a single surgeon and single prosector at necropsy.

For the short-term study, animals were followed for 28 days postoperatively with focused sampling and analysis based on immunologic parameters. Animals underwent blood sampling every 2-3 days for the first 2 weeks postoperatively and weekly for the last 2 weeks postoperatively. VAT and SAT were collected during surgery and at necropsy (Figure 5A).

Blinding occurred during data analysis when feasible; specifically, experimenters were blinded during analysis of immunohistochemistry including cell counting and morphometric analysis, as well as during microbiome and metabolome assays. Due to clinical care requirements, experimenters could not be blinded to whether the animal received sham surgery or VSG for the other aspects of the experiment including weights, caloric intake, and metabolic characterization. The experimenters performing data analysis were not involved in daily care of animals and raw data collection, providing an additional level of removal from unblinded data collection prior to analysis.

Surgical technique

Anesthesia. All animals were fasted the evening prior to and the morning of surgery. Animals were premedicated with pregabalin (100 mg *per os* [PO]) to enhance analgesia in the postoperative period and ondansetron (4 mg PO) to reduce postoperative nausea. Anesthesia was induced using ketamine (5-15 mg/kg intramuscular [IM]) and midazolam (0.1-0.5 mg/kg IM). Preoperative analgesia included buprenorphine (0.03 mg/kg IM), ketoprofen (1 mg/kg IM), and local infiltration of 0.25% bupivacaine at intended incision sites. Animals were endotracheally intubated and mechanically ventilated. Anesthesia was maintained with inhaled isoflurane. Anesthetic parameters including electrocardiography, pulse oximetry, end tidal CO_2, heart rate, blood pressure, temperature, and respiratory rate were monitored throughout the procedure.

Buprenorphine (0.01-0.03 mg/kg IM twice daily) and ketoprofen (1 mg/kg IM once daily) were administered for 72 hours postoperatively for analgesia. On D3-D5, analgesia was transitioned to acetaminophen (5-15 mg/kg PO twice daily). No breakthrough pain was observed during postoperative care.

Surgical technique. All surgical procedures were performed by an experienced bariatric surgeon. No perioperative antibiotics were utilized in this protocol. After induction of anesthesia, the animals were placed in a slight reverse Trendelenburg position using padding. Hair was shaved from the abdomen and lower chest. Animals were prepped using chlorhexidine scrub (Chloraprep, BD, Franklin Lakes, NJ, USA) and draped in the standard sterile fashion. For animals assigned to receive the sham surgery, intended port sites were infiltrated with local anesthetic and a 12-mm incision was made above the umbilicus to the left of midline. A biopsy of SAT was taken from this incision. Under direct vision, a 12-mm port was placed through this incision into the abdomen and pneumoperitoneum was established to 8 mm Hg with carbon dioxide. Throughout the procedure the abdomen was insufflated for 10-minute intervals with 30-second rest periods to allow for maintenance of normal physiology. After laparoscopic inspection of the abdomen, four additional ports were placed: a 12-mm port above the umbilicus to the right of midline, a 5-mm port in the right upper quadrant of the abdomen, a 5 -mm port in the right lateral abdomen, and a 5-mm port in the left lateral abdomen. An omental biopsy of VAT was obtained utilizing a laparoscopic ultrasonic dissection device (Figure 1C, Sonicision™, Medtronic, Minneapolis, MN). The liver was retracted cephalad, and beginning 4 cm from the pylorus of the stomach the gastro-colic fat was divided from the greater curvature of the stomach utilizing the ultrasonic dissection device (Figure 1C). The greater curvature and posterior wall of the stomach were completely freed from omental fat and fibrous adhesions up to the gastroesophageal junction. A 9.6 mm pediatric gastroscope (Olympus Medical System®, Tokyo, Japan) was then introduced into the stomach and passed into the duodenal bulb. At this point, sham

procedures were concluded with withdrawal of the gastroscope, desufflation of pneumoperitoneum, removal of the trocars, closure of the anterior fascia of the 12 mm port sites using 4-0 PDS suture (Ethicon, Somerville, NJ), closure of all skin incisions using 5-0 Monocryl subcuticular stitches (Ethicon), and application of topical skin adhesive over all incisions (Dermabond, Ethicon).

For animals assigned to receive VSG, procedures were continued after introduction of the gastroscope with removal of the greater curvature of the stomach along the gastroscope. This was performed by sequential stapling starting 4 cm from the pylorus and extending toward the angle of His with an Endo GIA^{TM} stapling device and purple staple loads (Medtronic, Minneapolis, MN, USA) (Figures 1E–1G). Three staple loads were used to create the sleeve gastrectomy. The gastroscope was withdrawn and the entire staple line was visualized endoscopically (Figure 1I). The divided gastric specimen was removed from the left upper quadrant 12 mm port (Figures 1B and 1H). In the long-term study, a leak test was performed by insufflating the stomach with the gastroscope and submerging the stomach under sterile saline to identify any leakage with the laparoscopic view; no leaks were identified in any animal. Leak testing was not performed in the short-term study. Following removal of the gastroscope, the abdomen was desufflated and closed as described above.

Postoperative care. Immediately postoperatively (24-48 hours), animals were offered a completely liquid diet (Ensure Clear, Abbott Nutrition, Lake Forest, IL, USA). On D2, diet was advanced to mashed standard biscuits and pureed enrichments. For the long-term study, on D42 animals were progressed to regular biscuits and enrichments. Paired sham and VSG animals were offered identical diet choices, including matched enrichment offerings to ensure matched caloric offerings up to D180. Following D180, animals in both groups were switched to an ad lib feeding paradigm and offered access to an excess of biscuits. Intake in kcal/kg/day was recorded daily for each animal.

Animal morphometric evaluation

Weights were obtained at least twice weekly. For the long-term study, umbilical circumference and BCS were measured at the time of the operation and at 45, 90, and 365 days postoperatively (Clingerman and Summers, 2005).

Glucose tolerance testing

Prior to metabolic testing, animals were fasted for at least 10 and not more than 16 hours. For IVGTT, $\leq$25% dextrose (0.5 g/kg) was injected and the VAP was immediately flushed with normal saline at 10x port and catheter volume to assure there was no residual dextrose contamination in subsequent samples, and blood was collected at multiple timepoints (3x baseline, 1, 3, 5, 7, 10, 15, 20, 25, 30, and 60 minutes) in awake, cooperating animals. Additional glucose measurements at 15, 20, 25, 30, and 60 minutes were obtained via heel stick. During the initial preoperative OGTT animals were given a 4 g/kg oral solution, which was poorly tolerated so the glucose dose was decreased to 1.75 g/kg (consistent with the dose for human pediatric testing), for subsequent OGTTs. There is no consistent weight-dependent or fixed glucose dose in the literature for OGTT in primates. Blood samples for glucose measurement were collected at baseline, 30, 60, 90, 120, 150, and 180 minutes.

HOMA-IR was calculated from fasting c-peptide levels using the modified formula from Basukala et al. (Basukala et al., 2018), as this has greater sensitivity than using fasting insulin levels: HOMA-IR = 1.5 + FPG × FCP / 2800 where FPG = fasting plasma glucose (mmol/L) and FCP = fasting c-peptide (pmol/L). Unit conversions were as follows: glucose mg/dL x 0.0555 = glucose mmol/L; c-peptide ng/mL x 0.333 = c-peptide nmol/L (2018).

Laboratory testing

Point-of-care glucose measurements were made using a standard glucometer (Nova Biomedical, Waltham, MA, USA). HgbA1c was measured from whole blood using a point-of-care DCA Vantage Analyzer (Siemens Healthineers USA, Malvern, PA, USA). For C-peptide and incretin assays, venous blood was collected into serum separator tubes treated with bovine lung aprotinin (Millipore-Sigma, Darmstadt, Germany) at a ratio of a minimum of 500 kU to 1 mL of sample. Incretins were measured using the Non-Human Primate Metabolism Multiplex Assay (Millipore-Sigma, Darmstadt, Germany) using an automated Olympus Au400e analyzer (Olympus America, Melville, NY, USA). C-peptide was measured via radioimmunoassay (Millipore-Sigma, Darmstadt, Germany) using the Genesys Genii instrument (Laboratory Technologies, Elburn,

IL, USA). For complete blood counts, venous blood samples were collected into EDTA-treated microtainers and analyzed using the Advia 2120 hematology analyzer (Siemens Healthineers USA, Malvern, PA, USA). For chemistry panels, lipid levels, and metabolomics, venous blood samples were collected into serum separator tubes and centrifuged to obtain serum. Chemistry panels were analyzed using an AU480 chemistry analyzer (Beckman Coulter, Brea, CA, USA). Lipid levels were analyzed via NMR spectroscopy at Marshfield Labs (Marshfield, WI, USA).

The glucose disappearance rate ($K_{glucose}$) was calculated as the slope of the decline of the log-transformed blood glucose between 10 and 30 minutes. HOMA-IR was calculated from fasting c-peptide levels using the modified formula from Basukala et al. (Classification and diagnosis of diabetes. Sec. 2, 2015; Basukala et al., 2018).

Metabolomics. Untargeted/shotgun metabolomics on peripheral serum was performed by Metabolon, Inc. (Morrisville, NC, USA). Peripheral serum was collected as above and stored at -80°C until use. Samples were prepared using the automated MicroLab STAR system (Hamilton Company, Reno, NV, USA). Proteins were precipitated with methanol under vigorous shaking for 2 min followed by centrifugation to recover protein-bound metabolites and remove proteins. The resulting extract was analyzed with separate ultra-performance liquid chromatography (UPLC)-tandem mass spectroscopy (MS) methods as follows: reverse phase (RP) UPLC-MS/MS with positive ion mode electrospray ionization (ESI) chromatographically optimized for more hydrophilic compounds, RP/UPLC-MS/MS with positive ion mode electrospray ionization (ESI) chromatographically optimized for more hydrophobic compounds, RP/UPLC-MS/MS with negative ion mode ESI, and hydrophilic interaction liquid chromatography (HILIC)/UPLC-MS/MS with negative ion mode ESI. Raw data was extracted, peak-identified, and QC processed by Metabolon, Inc.; metabolites were identified by comparison to an internal library of purified standards, resulting in a total list of 795 metabolites. Data were normalized in terms of raw area counts, missing values were imputed with the minimum, and data was then rescaled to set the median equal to one. Data are presented as fold change of the VSG group to the sham surgery group at each timepoint.

Targeted/quantitative metabolomics on peripheral serum was performed by Metabolon, Inc. to quantify BAs and SCFAs utilizing commercial liquid chromatography (LC)-MS/MS. The Bile Acid Panel has the capacity to measure major primary and secondary BAs and conjugates: cholic acid, chenodeoxycholic acid, deoxycholic acid, lithocholic acid, ursodeoxycholic acid, glycocholic acid, glycochenodeoxycholic acid, glycodeoxycholic acid, glycoursodeoxycholic acid, taurocholic acid, taurochenodeoxycholic acid, taurodeoxycholic acid, taurolithocholic acid, tauroursodeoxycholic acid, and glycolithocholic acid. Protein precipitation of standards, QC samples, and experimental samples was performed with acidified methanol and centrifugation, followed by drying of the resultant supernatant with a nitrogen stream. The dried extracts were reconstituted and analyzed with RP/UPLC/MS-MS with negative ion mode ESI on an Agilent 1290 Infinity/SCIEX QTRAP 6500 LC-MS/MS system (Santa Clara, CA, USA). The SCFA panel has the capacity to measure acetic acid, propionic acid, isobutyric acid, butyric acid, 2-methyl-butyric acid, isovaleric acid, valeric acid, and hexanoic acid. Standards are prepared at 8 different concentrations. The methodology for this panel was similar to that of the BA panel, with protein precipitation with an organic solvent and centrifugation. An aliquot of the resultant supernatant was directly analyzed with RP/UPLC/MS-MS with negative ion mode ESI on an Agilent 1290 Infinity/SCIEX QTRAP 5500 LC-MS/MS system. For both panels, the peak area for each metabolite was determined and quantitation was performed using a weighted linear least squares regression analysis generated from calibration standards. Values below the limit of quantification were imputed with the lower limit of quantification. Data are presented as fold change of the VSG group to the sham surgery group at each timepoint to generate a heat map, or as quantitative values (ng/mL) for selected metabolites.

Microbiome. DNA was extracted from NHP feces using the DNeasy PowerSoil isolation kit. Fresh fecal samples were collected after morning cage cleaning from pans that were disinfected and dried for this purpose. Libraries for whole genome shotgun sequencing were prepared using $^1/_4$ NexteraXT reactions (Hillmann et al., 2018), and paired end sequencing was performed at a read length of 150 nt on the Illumina MiSeq platform by the University of Minnesota Genomics Center (Minneapolis, MN, USA). Negative (sterile water) controls were included. Taxonomic annotations of sequence data were done using MetaPhlAn 2 version 2.6.0 (Truong et al., 2015).

Adipose tissue processing for conventional flow cytometry. VAT was broken up using sterile forceps and the pieces were submerged in serum-free dissociation buffer (IMDM with 1 mM glutathione, 1 U/mL

Heparin Sodium, 0.1 mg/mL DNAse I, 0.8 mg/mL Dispase II (Roche, Basel, Switzerland), and 0.2 mg/mL Collagenase IV). Following 30 minutes at 37°C, the tissue was triturated and centrifuged three times to obtain the SVF. A single cell suspension was made by passing the resuspended pellet through a 70 μm mesh filter. This suspension was stained with antibodies against CD45 to identify hematopoietic cells, CD3, CD19, and CD56 to identify T, B, and NK cells. CD64 and CD163, MERtk, CD169, CD11b, CD11c, CD16, CD14, and CD123 antibodies were used to mark macrophages, monocytes, neutrophils, and eosinophils. Macrophage subsets were delineated by analyzing the expression of HLA-DR and CD40 (M1) versus CD206 (M2).

Immunohistochemistry and adipocyte morphometry. Immunohistochemistry was performed on VAT and subcutaneous adipose tissue (SAT) collected at the time of surgery and at necropsy one year after VSG. Tissue was fixed with 10% formalin and paraffin-embedded. Four-μm thick sections of adipose tissue were cut and slides were loaded onto the Biocare Intellepath IHC staining instrument (Biocare Medical, Pacheco, CA, USA). For IBA-1 staining, antigen retrieval was performed by incubation with citrate buffer (Agilent Dako, Santa Clara, CA, USA) for 30 minutes at 97°C. Slides were blocked (Dako protein block, catalog #X090930-2, Agilent Dako) for 15 minutes at room temperature, stained with polyclonal goat anti-IBA-1 antibody (polyclonal, 1:1000, catalog #ab107159, Abcam, Cambridge, MA, USA) for 30 minutes at room temperature, followed by detection by goat-on-rodent HRP-polymer detection antibody kit (Biocare Medical) for 15 minutes at room temperature with the probe and 20 minutes at room temperature with the polymer. For CD3 staining, antigen retrieval was performed by incubation with EDTA (Agilent Dako) for 30 minutes at 97°C. Slides were blocked (Dako protein block, catalog #X090930-2, Agilent Dako) for 15 minutes at room temperature, stained with CD3 rat anti-human antibody (clone CD3-12, 1:1000, catalog #S2367, Bio-Rad, Hercules, CA, USA) for 30 minutes at room temperature, followed by incubation with rat-on-mouse HRP-polymer detection antibody kit (Biocare Medical) for 15 minutes at room temperature with the probe and 20 minutes at room temperature with the polymer. Slides were visualized with DAB substrate (Agilent Dako) and counterstained with hematoxylin (Agilent Dako), incubated for 5 minutes at room temperature each.

For CLS density and adipocyte volume, IBA-1-stained slides were digitized at 40x using the Motic EasyScan Digital Slide Scanner and corresponding Motic EasyScanner software (Motic, British Columbia, Canada). Five randomly selected, non-overlapping images were captured at 10x magnification from each digitized slide using Aperio ImageScope software (Leica Biosystems, Vista, CA, USA) for analysis using ImageJ (imagej.nih.gov). A total of 100 adipocytes were manually traced in ImageJ from each image set using a drawing tablet. CLSs in the classic conformation (see Figure 1J) were manually counted from the images used to trace the 100 adipocytes. For calculating adipocyte volume, the diameter of each traced adipocyte was derived from the adipocyte area given by ImageJ based on the assumption that the cells are spherical (Goldrick, 1967). Adipocyte volume was calculated with the following formula from Goldrick et al.: $(\pi/6)(3\sigma^2+ x^2)x$ where σ^2 is variance of the diameter and x is the mean diameter (Cinti et al., 2001, 2005; Goldrick, 1967). Morphometry and CLS density evaluation were performed by two trained individuals for each slide.

For $CD3^+$ cell counts, each CD3-stained slide was analyzed blindly by two pathologists. CD3-stained cells were counted on each slide from 15 randomly selected, non-overlapping high-powered (400x) fields. Data are expressed as a delta change from day of surgery to allow for appropriate representation of null counts.

Adipose tissue and blood processing for CyTOF. Approximately 6-8 g of VAT and 3-5 g of SAT collected at D0 and D28 after VSG for the short-term study were minced and digested in 0.5 mg/mL collagenase II (Worthington Biochemical, Lakewood, NJ, USA) at 37°C for 45 min, passed through a 100 μm cell strainer, and centrifuged to obtain SVF cells. SVF cells were resuspended in 2 mL red blood cell lysis buffer (STEMCELL Technologies, Vancouver, Canada), incubated, and washed with PBS followed by cRPMI. PBMCs collected longitudinally were obtained by density gradient centrifugation of 4-5 mL of whole venous blood.

CyTOF staining, data acquisition, and preprocessing. Purified antibodies were labeled in-house with corresponding metal tags using Maxpar® Antibody Labeling Kits (Fluidigm) as per manufacturer's instructions and titrated to determine the working concentration.

Cryopreserved cells (SVF and PBMCs) were immediately thawed from liquid nitrogen storage at 37°C in a water bath. Cells were washed with cRPMI followed by three washes in barium-free PBS by spinning at

1200 rpm for 5 minutes. One to two million cells from each sample were stained with cell ID Cisplatin (^{194}Pt, ^{198}Pt) to a final concentration of 1 μM for 5 min at room temperature to label dead cells. Human TruStain FcX Fc receptor blocker (BioLegend, San Diego, CA, USA) was used to block nonspecific Fc binding, followed by incubation with 50 μL of cell surface antibodies cocktail in MaxPar Cell Staining Buffer (CSB) at 4°C for 30 minutes. After incubation, cells were washed twice in CSB and fixed as described above, followed by two washes in MaxPar Perm-S buffer for permeabilization. Fifty μL of the antibodies cocktail against intracellular targets (PPARγ, Ki67, FoxP3 and Tbet) were incubated with permeabilized cells in Perm-S buffer for 30 minutes at 4°C. At the end of the staining, cells were washed twice in CSB and stored in 1 mL of MaxPar Fix and Perm Buffer containing 125 nM MaxPar Intercalator-Ir (^{191}Ir and ^{193}Ir) at 4°C. After 12 h (overnight), cells were washed twice in CSB.

Immediately before data acquisition, samples were washed twice with PBS, twice in MaxPar water, filtered through a 35-μm membrane, and resuspended at a concentration of 0.5 × 10^6 cells/mL in 10% EQTM four element calibration beads (Fluidigm). The samples were acquired on a CyTOF® 2 Mass Cytometer (Fluidigm) at an event rate of 500 event/second with noise deduction. To minimize the batch effect, samples were stained in one batch then analyzed by CyTOF in one day. Before downstream analysis, FCS files were normalized with CyTOF software 6.7 (Fluidigm).

CyTOF data analysis dimensionality reduction and clustering. Normalized FCS files were submitted to Cytobank for gating and viSNE analysis. Manual gating was performed to identify cell events ($^{191/193}$Ir/DNA^{hi}) and exclusion of dead or dying cells ($^{194/198}$Cis$^+$). The CD45$^+$ live cells were left for subsequent enumeration of immune cells frequency by Cytobank or FlowJo 10.7.1 (BD Biosciences, Franklin Lakes, NJ, USA) and tSNE or FlowSOM clustering analysis with FlowJo 10.7.1 plugins (Figure S6). CD45$^+$ events were used for gating CD3$^-$CD20$^-$ myeloid cells and CD25$^+$CD127$^-$ Tregs from pre-gated CD3$^+$CD4$^+$ T cells events (Figure S6). After applying quality control measures to each sample (n=12), we concatenated individual FCS files (PBL_D0, PBL_D28, SAT_D0, SAT_D28, VAT_D0 and VAT_D28) from both animals into a single FCS file. Care was taken to ensure that each sample contributed equal numbers of cells (2200 events/sample from myeloid cells and 420 events from CD25$^+$CD127$^-$/of CD4$^+$ T cells) to this dataset to avoid having the largest samples dominate the analysis and confound association phenotype. After sampling an equal number of cells from each sample, we grouped these cells into D0 and D28 for PBLs, SAT and VAT (Figure S7).

The concatenated file of a total of 26,400 myeloid cells was used to conduct tSNE using default settings (auto: opt-SNE) with 29 immune parameters (CD45, CD14, CD16, CD11c, CD206, CD68, CD123, CD141, CD163, CD95, CD38, CD11b, CD33, PPARγ, Tbet, Ki67, FoxP3, CD2, CD24, CD25, CD27, CD40, CD103, LAG-3, CD49b, CD69, CD107a, CD127, and HLA-DR) as the clustering channels. The above same channels were used to generate 12 unique, Phenograph-guided FlowSOM populations/clusters on each group of samples by FlowJo Plugins (Phenograph v2.4 and FlowSOM v2.9) and overlay on tSNE map for data visualization. FlowSOM-generated frequency of all 12 myeloid population and MFI of each channel on these population are presented.

Similarly, tSNE (auto: opt-SNE) was run on the concatenated file of 2,200 Tregs with 20 immune parameters (CD4, CD25, CD127, FoxP3, PPARγ, LAG-3, CD49b, Ki67, CD27, CD28, CD40, CD11b, CD11c, CD69, Tbet, CD95, CD103, CD107a, CD38, and HLA-DR) as the clustering channels. The above same channels were used to generate six unique, Phenograph-guided FlowSOM populations/clusters of Tregs on each group of samples using FlowJo Plugins (Phenograph v2.4 and FlowSOM v2.9) and overlay on tSNE map for data visualization. FlowSOM-generated frequency of all six Tregs population and MFI of each channel on these population are presented.

QUANTIFICATION AND STATISTICAL ANALYSIS

Values are reported as mean ± standard error of the mean (SEM) unless otherwise specified. Statistical analysis was performed using Prism version 8.0 (GraphPad Software, San Diego, CA, USA) with the exception of microbiome analysis, which was performed on Microsoft Excel 2018 (Redmond, WA, USA). All other data were assessed using unpaired two-tailed Student's t tests (De Winter, 2013) with a significance level (α) of 0.05. Data are presented as mean ± SEM, and significance denoted as: *p<0.05, **p<0.005, #p=0.05. Multiple comparisons were not accounted for as each sample was taken independently of others. Data normality was assumed and not tested given small sample size.